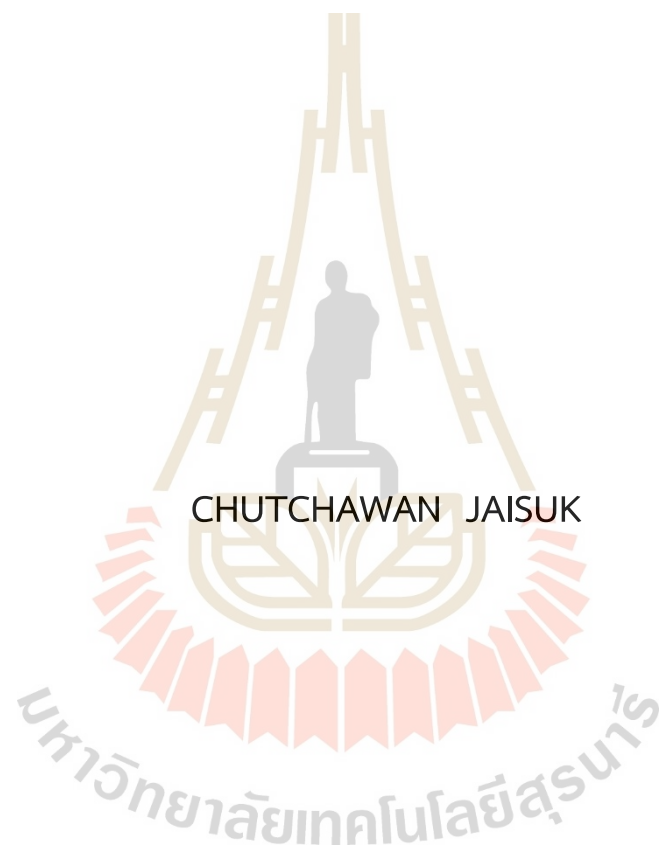


SHIFTING OF THE CHEMICAL POTENTIAL IN A STRONGLY
CORRELATED MATERIAL: THE CASE OF NICKEL OXIDE



CHUTCHAWAN JAISUK

A Thesis Submitted in Partial Fulfillment of the Requirement for the
Degree of Doctor of Philosophy in Physics
Suranaree University of Technology
Academic Year 2022

การเปลี่ยนแปลงศักย์เคมีใน Strongly Correlated Material:
นิกเกิลออกไซด์ (กรณีศึกษา)



วิทยานิพนธ์นี้เป็นส่วนหนึ่งของการศึกษาตามหลักสูตรปริญญาวิทยาศาสตรดุษฎีบัณฑิต
สาขาวิชาฟิสิกส์
มหาวิทยาลัยเทคโนโลยีสุรนารี
ปีการศึกษา 2565

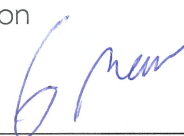
SHIFTING OF THE CHEMICAL POTENTIAL IN
A STRONGLY CORRELATED MATERIAL: THE CASE OF NICKEL OXIDE

Suranaree University of Technology has approved this thesis submitted in partial fulfillment of the requirements for the Degree of Doctor of Philosophy.

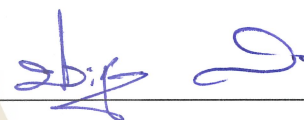
Thesis Examining Committee



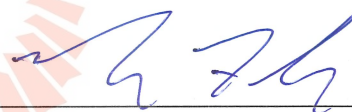
(Assoc. Prof. Dr. Panomsak Meemon)
Chairperson



(Assoc. Prof. Dr. Worawat Meevasana)
Member (Thesis Advisor)



(Assoc. Prof. Dr. Prayoon Songsiriritthigul)
Member



(Asst. Prof. Dr. Michael F. Smith)
Member



(Dr. Hideki Nakajima)
Member



(Assoc. Prof. Dr. Yupaporn Ruksakulpiwat)
Vice Rector for Academic Affairs
and Quality Assurance



(Prof. Dr. Santi Maensiri)
Dean of Institute of Science

ชัชวาล ใจสุข : การเปลี่ยนแปลงศักย์เคมีใน Strongly Correlated Material: นิกเกิลออกไซด์ (กรณีศึกษา) (SHIFTING OF THE CHEMICAL POTENTIAL IN A STRONGLY CORRELATED MATERIAL: THE CASE OF NICKEL OXIDE). อาจารย์ที่ปรึกษา : รองศาสตราจารย์ ดร.วรวัดน์ มีวาสนา, 60 หน้า.

คำสำคัญ: ศักย์เคมี, วัสดุกลุ่มที่มีอันตรกิริยา correlation ขั้นสูง, ชนวนไฟฟ้าประเภท MOTT, ชนวนไฟฟ้าประเภท CHARGE TRANSFER, นิกเกิลออกไซด์

ศึกษาเชิงทดลองโครงสร้างทางอิเล็กทรอนิกส์ของนิกเกิลออกไซด์ (NiO) โดยใช้โฟโตมิชชันสเปกแบบแยกแยะเชิงมุม (ARPES) การวิเคราะห์ ARPES เผยให้เห็นการเปลี่ยนแปลงเชิงลบในศักย์สารเคมี ซึ่งบ่งชี้ถึงความสามารถในการบีบอัดทางอิเล็กทรอนิกส์เชิงลบ ($dp/dn < 0$) ทั้งนี้เพื่ออธิบายถึงประโยชน์ของการใช้ strongly correlated materials ในการใช้งานการเก็บพลังงาน จึงได้จำลองการเปลี่ยนแปลงศักย์เคมีที่อาจเกิดขึ้นใน Mott-insulator ภายใต้การเจือด้วยประจุตัวนำ โดย Mott-gap จะหดสั้นลงเมื่อถูกเจือมากขึ้น ส่งผลให้ศักย์สารเคมี (μ) จะมีการเปลี่ยนแปลงช้ากว่าปกติ ซึ่งปรากฏการณ์นี้ช่วยเพิ่มความสามารถในการเก็บประจุของวัสดุได้อย่างมาก เพื่อตรวจสอบความถูกต้องของแนวคิดนี้ จึงได้สำรวจความจุของประจุของอิเล็กโทรดที่มีทองแดง (Cu) แมงกานีส (Mn) โคบอลต์ (Co) และเหล็ก (Fe) ตามรายงานการวิจัย ซึ่งแสดงให้เห็นว่าสถานะ Mott-insulator มีประสิทธิภาพสูงกว่าตัวฉนวนแบบทั่วไปในแง่ของความจุในการเก็บประจุ ยิ่งไปกว่านั้น สถานะ the intermediate state ออกซิเดชันที่สูงขึ้นเล็กน้อยของอะตอมของโลหะทรานซิชัน แสดงความจุของประจุสูงสุดเนื่องจากการครอบคลุมพื้นที่การยับยั้งการเปลี่ยนแปลงของศักย์เคมีที่มากกว่า การศึกษา นี้แสดงให้เห็นถึงข้อสนับสนุนการใช้ประโยชน์ของวัสดุกลุ่ม strongly correlated materials สำหรับการใช้งานเชิงกักเก็บพลังงาน พร้อมกันนี้ความเข้าใจที่ได้มาเป็นการปูทางไปสู่การพัฒนาาระบบกักเก็บพลังงานที่ปรับปรุงให้ดีขึ้นโดยใช้คุณสมบัติเฉพาะของวัสดุกลุ่ม strongly correlated materials

สาขาวิชาฟิสิกส์
ปีการศึกษา 2565

ลายมือชื่อนักศึกษา

ชัชวาล ใจสุข

ลายมือชื่ออาจารย์ที่ปรึกษา

Dr. W. Wattana

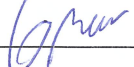
CHUTCHAWAN JAISUK : SHIFTING OF THE CHEMICAL POTENTIAL IN A STRONGLY CORRELATED MATERIAL: THE CASE OF NICKEL OXIDE. THESIS ADVISOR : ASSOC. PROF. WORAWAT MEEVASANA, Ph.D. 60 PP.

Keyword: CHEMICAL POTENTIAL SHIFTING, STRONGLY CORRELATED MATERIAL, MOTT-INSULATOR/CHARGE TRANSFER INSULATOR, NICKEL OXIDE

This experimental study investigates the electronic structure of strongly correlated nickel oxide (NiO) during electron doping using angle-resolved photoemission spectroscopy (ARPES). Our ARPES analysis reveals a negative shift in the chemical potential, indicating negative electronic compressibility ($d\mu/dn < 0$). To elucidate the benefits of employing strongly correlated materials in energy storage applications, we introduce a model of chemical potential suppression observed in doped Mott insulators. As the Mott gap diminishes upon doping, the chemical potential (μ) experiences suppression, gradually increasing in value. This phenomenon significantly enhances the charge storage capability of the material. To validate this concept, we explore the charge capacity from the discharge profiles for copper (Cu), manganese (Mn), cobalt (Co), and iron (Fe) based electrodes based on the research report. Our findings demonstrate that the Mott state surpasses conventional band insulators in terms of charge storage capacity. Furthermore, the intermediate state, slightly shifted to higher oxidation states of transition metal atoms, exhibits the highest charge capacity due to the optimal utilization of chemical potential suppression. This study provides valuable evidence supporting the benefits of strongly correlated materials for energy storage applications. The acquired understanding paves the way for the development of enhanced energy storage systems by utilizing the unique properties of strongly correlated materials.

School of Physics
Academic Year 2022

Student's Signature
Advisor's Signature

Chutchawan Jaisuk


ACKNOWLEDGEMENTS

I would like to express my heartfelt gratitude to all those who have contributed to the completion of this thesis. Their support, encouragement, and guidance have been instrumental in shaping my research journey.

First and foremost, I am deeply indebted to my thesis advisor, Assoc. Prof. Dr. Worawat Meevasana. I am deeply grateful their unwavering support, motivation, and inspiration throughout this academic journey. I would also like to extend my appreciation to the members of my thesis committee, Assoc. Prof. Dr. Panomsak Meemon, Assoc. Prof. Dr. Prayoon Songsiritthigul, Asst. Prof. Dr. Michael F. Smith, and Dr. Hideki Nakajima for their valuable time, expertise, and insightful suggestions. Their constructive comments and critical analysis have significantly enhanced the quality of this thesis.

I am thankful to the contributions of my colleagues and classmates in Meevasana group who have supported me throughout this journey. Their intellectual discussions, collaboration, and friendship have made this research experience enriching and enjoyable.

I would like to acknowledge the Development and Promotion of Science and Technology Talents Project (DPST- scholarship) for their generous financial support during the course of this thesis. I am truly thankful for the opportunities they have provided me to pursue my educational goals.

I am grateful to my family for their unwavering love, encouragement, and belief in my abilities. Their constant support and understanding have been the driving force behind my academic pursuits.

In conclusion, this thesis would not have been possible without the contributions and support of all those mentioned above. I am truly grateful for their involvement in this research journey.

Chutchawan Jaisuk

CONTENTS

	Page
ABSTRACT IN THAI.....	I
ABSTRACT IN ENGLISH.....	II
ACKNOWLEDGEMENTS	III
CONTENTS.....	IV
LIST OF TABLES	VI
LIST OF FIGURES	VII
CHAPTER	
I INTRODUCTION	1
1.1 Background and motivation	1
1.2 Research objectives	3
1.3 Outline of thesis	3
II LITERATURE REVIEWS.....	4
2.1 Mott-insulator.....	4
2.2 Nickle Oxide (NiO).....	7
2.3 Chemical potential shift.....	10
2.3.1 Chemical potential pinning.....	10
2.3.2 Negative Electron Compressibility (NEC).....	13
2.4 Photoelectric Effect.....	14
2.5 Angle Resolved Photoemission Spectroscopy (ARPES)	15
2.6 Energy storage.....	19
2.7 Electrochemical Measurements on Electrode Materials.....	21
2.7.1 Cyclic Voltammety (CV).....	22
2.7.2 Galvano static charge–discharge (GCD).....	24
III ANGLE-RESOLVED PHOTOEMISSION SPECTROSCOPY ON STRONGLY CORRELATED MATERIAL: THE CASE OF NICKEL OXIDE (NIO)	27
3.1 NiO sample	27
3.2 Experimental Angle-Resolved Photoemission Spectroscopy	29
3.3 Synchrotron Facilities.....	30
3.4 Angle-Resolved Photoemission Spectroscopy Data.....	30
3.5 DFT calculation	31

CONTENTS (Continued)

	Page
IV ARPES RESULT	34
4.1 ARPES background subtraction	34
4.2 Processed ARPES data	37
V INVESTIGATION OF BATTERY ELECTRODE PERFORMANCE (STRONGLY CORRELATED MATERIALS FRAMEWORK)	40
5.1 The Hypothesis	40
5.2 Copper based electrodes (CuO, Cu ₂ O)	42
5.3 Manganese based electrodes (MnO, Mn ₃ O ₄ , and MnO ₂).....	44
5.4 Cobalt based electrodes (CoO, Co ₃ O ₄) and Iron based electrodes (Fe ₂ O ₃ , Fe ₃ O ₄)	46
5.5 Discussion on chemical potential shifting	49
IV CONCLUSION AND FUTURE RESEARCH	51
6.1 Conclusions.....	51
6.2 Improvement and future research.....	52
REFERENCES	53
APPENDIX.....	57
CURRICULUM VITAE.....	60

LIST OF TABLES

Table	Page
5.1 The calculated charge storage capacity of Cu-based electrodes.....	43
5.2 The calculated charge storage capacity of Mn-based electrodes.....	45
5.3 The calculated charge storage capacity of Co-based electrodes.....	47
5.4 The calculated charge storage capacity of Fe-based electrodes.....	48



LIST OF FIGURES

Figure	Page
1.1 Schematic of Mott-gap closing scenario	1
2.1 Schematic phase diagram of high-T _c superconductors presents hole doping LSCO (right) and electron doping NCCO (left) (Lee et al., 2006).....	5
2.2 Schematic phase diagram of La _{1-x} Ca _x MnO ₃	6
2.3 The typical rock salt structure of NiO (red and white color represent Ni and O atom, respectively).....	8
2.4 XPS and BIS spectra of NiO presenting the 4.3 eV band gap (Sawatzky et al., 1984)	9
2.5 Electronic structure of NiO observed by XPS and BIS and assigned states in the Mott-Hubbard Picture (Sawatzky et al., 1984)	9
2.6 Zaanen–Sawatzky–Allen U–Δ plot for transition-metal oxides. The given compounds are classified either in the Mott–Hubbard in the regime (Δ>U) or in the charge-transfer regime (U>Δ) (Fujimori et al., 2002).....	10
2.7 Chemical Potential Shift in hole doped LSCO and LSNO (Satake et al., 2000)....	11
2.8 Chemical Potential Pinning in PCMO (Ebata et al., 2008).....	12
2.9 The electronic structure evolution on electron doping in strongly correlated (Sr _{1-x} La _x) ₃ Ir ₂ O ₇ . As electron doping increases from x = 0.035 to x = 0.083, the valence band top move upward, while the conduction band bottom move downward resulting in effective lowering of Δμ in the NEC scenario (Hu et al., 2015).....	13
2.10 Photoelectric phenomena for simple explanation.....	14
2.11 The fundamental principle of Angle-resolved photoemission spectroscopy (ARPES) measurement. The top panel illustrates the geometry of ARPES measurement. As the photon (red line) incident into sample, the electron are ejected from the sample surface (blue line) and collected by electron analyzer. The bottom panel presents the momentum conservation of electrons. The in-plane momentum (k) is conserved, while the perpendicular to the surface is not conserved (Baiqing Lv et al., 2019)	16
2.12 A schematic of energy level of photoelectron in ARPES measurement. The energy is conserved associated with equation (1) (Baiqing Lv et al., 2019)	16

LIST OF FIGURES (Continued)

Figure	Page
2.13 The Illustration of three-step crucially used for describing the possible photoemission process.....	17
2.14 Schematic of Li-ion battery (LIB) consists of a negative electrode (graphite), positive electrode (LiCoO ₂), current collectors, liquid electrolyte and separator. Li-ions move from the positive (negative) electrode to the negative (positive) electrode through the electrolyte during charging (discharging); while electrons simultaneously travel through an external circuit to ensure charge balance (Zhang et al., 2017).....	19
2.15 Schematic energy level in Li-ion Battery (Hausbrand et al., 2015).....	20
2.16 The operating potential and capacity of battery electrode (from https://www.eai.in/blog/2018/12/research-status-of-anode/cathode-material.html).	21
2.17 The voltage profile applied in CV measurement (Yang et al., 2019).	22
2.18 Current response versus voltage curves in CV measurement (Yang et al., 2019).	23
2.19 The voltage versus integral current curves in CV measurement (Yang et al., 2019).	23
2.20 The current profile applied in GCD measurement (Yang et al., 2019)	24
2.21 The typical voltage response versus capacity in GCD measurement (Yang et al., 2019)	25
2.22 The differential capacity curve for charge and discharge in GCD measurement (Yang et al., 2019).....	25
2.23 The typical cycle stability of battery electrode (Yang et al., 2019)	26
2.24 The rate capability performance (Yang et al., 2019)	26
2.25 The Ragone diagram (Yang et al., 2019).	26
3.1 a) The crystal structure of NiO, the red and white color represent Nickel and Oxygen atom, respectively, b) The (100) plane of single crystal NiO with lattice constant 4.19 Å.....	27
3.2 Schematic of a) NiO single crystal sample preparation for ARPES measurement consisting of the sample holder and cleaving post attachment, b) the surface cleaving associated by applied external force to the cleaving post under vacuum condition, c) the side view, top view, and the actual sample.	28

LIST OF FIGURES (Continued)

Figure	Page
3.3 Schematic ARPES measurement: a) the photon (with energy $h\nu$) kicks the electron on the material surface out as the photoelectron and then collected by the electron analyzer, b) the hemisphere electron bend the trajectories of electrons entering a narrow slit at one end and interpret the final radius as the kinetic energy.....	29
3.4 The raw ARPES-spectra of graphite: a) kinetic energy versus angle, and b) binding energy versus momentum space.....	31
3.5 Schematic of the self-consistent field scheme for DFT calculation.	32
4.1 User interface panel present the selected area (above E_F) for MDC averaging....	35
4.2 the MDC background characterized from the averaged MDC spectrum above the Fermi-level. a) The averaged MDC background (red) is represented by the fitting curve (blue). b) The generated MDC curve for background subtraction from the fitting curve.....	35
4.3 User interface panel present the selected area for EDC averaging.....	36
4.4 The EDC background characterized from the averaged EDC spectrum in a specific momentum range. a) The averaged EDC background (red) is represented by the fitting curve (blue). b) The generated EDC curve for background subtraction from the fitting curve.....	37
4.5 Pre-processed (top panel) and Post-processed (bottom panel) ARPES data of the bare NiO, Potassium evaporation (for 20s and 40s), and UV-shinning treatment.....	38
4.6 The EDC present the relative shifting of the valence band a) the raw data b) the post processed data. Upon the alkaline metal evaporation, the valence band peak shift from the higher binding energy to lower binding energy. This changing in electronic structure is referred as the negative electronic compressibility	38
4.7 The valence band of NiO (100) in the $\bar{x} - \bar{\Gamma} - \bar{x}$, and 2D reciprocal space	39
5.1 The schematic of chemical potential changing.....	41
5.2 The re-reproduced the 2nd round of discharge profile of CuO (red-line) and Cu_2O (blue-line) electrode from experimental researches (Zhang et al., 2015)(Xiang et al., 2009)	43

LIST OF FIGURES (Continued)

Figure	Page
5.3 The Comparison of the charge storage capacity of CuO (Mott-insulator) and Cu ₂ O (Band-insulator) electrode (estimated from the reported charge/discharge profile of CuO (Zhang et al., 2015) and of Cu ₂ O (Xiang et al., 2009)	44
5.4 The re-reproduced the 60th round of discharge profile of MnO (red-line) and Mn ₃ O ₄ (green-line) and MnO ₂ (blue-line) electrode from experimental researches (Yue et al., 2014)	45
5.5 The Comparison of the charge storage capacity of MnO ₂ , Mn ₃ O ₄ and MnO electrode (estimated from the experimental reported charge/discharge profile of Manganese-base electrodes (Yue et al., 2014)).....	46
5.6 The re-reproduced the 2nd round of discharge profile of CoO (red-line) and Co ₃ O ₄ (green-line) electrode from experimental researches (Sun et al., 2017) ..	47
5.7 The re-reproduced the 2nd round of discharge profile of Fe ₂ O ₃ (green-line) and Fe ₃ O ₄ (red-line) electrode from experimental researches (Zhang et al., 2013)(Pan et al., 2018)	48
5.8 The Comparison of the charge storage capacity of (a) Cobalt-based electrode and (b) Iron-based electrode. The red candles (CoO and Fe ₃ O ₄) present the narrow Mott-sweeping, while the green candles (Co ₃ O ₄ and Fe ₂ O ₃) indicate the wide Mott-sweeping. The presented capacitances are normalized by that of the Mott-insulator.....	49
5.9 The schematic of chemical potential as a function of electron addition in manganese based electrodes	50
A Input file for PWscf calculation (Part I).....	58
B Input file for PWscf calculation (Part II).....	59
C Input file for band structure analysis.....	59

CHAPTER I

INTRODUCTION

1.1 Background and motivation

Strongly correlated material is a unique class in solid-state physics. These materials exhibit distinct characteristics due to the realistic behavior of electrons. The behavior of electrons in such materials is driven by a tendency to localize in order to minimize the total energy of the system. In other words, the electron tries to avoid the electron-electron repulsion. Describing the electronic structure of strongly correlated materials requires an approach different from the standard band theory used for conventional materials. One of the simplest and successful models for describing localized electrons in strongly correlated materials is the Hubbard model (Hubbard, 1963). The electronic structure of correlated electrons is determined by two fundamental parameters: the hopping parameter (t) and the on-site Coulomb repulsion (U). In cases of strong electron-electron interaction ($U > t$), the Hubbard model mathematically predicts the presence of a Mott gap. This gap arises from the splitting of the energy band into upper and lower Hubbard bands. The magnitude of the Mott gap is directly influenced by the strength of the electron-electron interaction in the system.

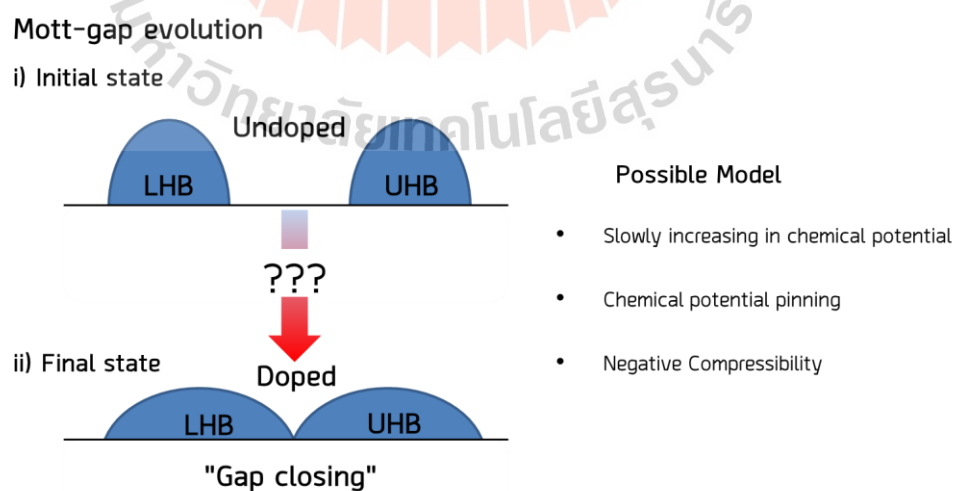


Figure 1.1 Schematic of Mott-gap closing scenario.

When strongly correlated materials undergo doping, the fundamental parameters (hopping parameter (t) and Coulomb interaction (U)) of the system will be modulated. In the case that the Coulomb interaction (U), or the ratio (U/t), is greatly reduced, the magnitude of the Mott gap will decrease toward zero. This evolution in electronic structure yields to the Mott-gap closing as illustrated in Figure 1.1. The experimental observations using Angle-resolved photoemission spectroscopy (ARPES) in electron-doped ($\text{Sr}_{1-x}\text{La}_x$) $_2\text{IrO}_4$ revealed the evolution of the Mott gap due to doping (De La Torre et al., 2015). This experiment identified the closure of the Mott gap at an electron doping concentration of approximately $x=5\%$. Similarly, the collapse of the Mott gap has been observed experimentally in the electron-doped $\text{Ca}_3\text{Cu}_2\text{O}_4\text{Cl}_2$ Mott-insulator (Hu et al., 2021). Furthermore, experimental ARPES on the Mott gap evolution in hole-doped ($\text{Sr}_{1-x}\text{K}_x$) $_2\text{IrO}_4$ demonstrated the closure of the Mott gap at a hole concentration of $x=3.5\%$ (Nelson et al., 2020). In term of chemical potential shifting, doping induced-Mott gap evolution will make an unconventional change in chemical potential as compare to the rigid band scenario. In this work, we would like to generalize the possibilities of chemical potential evolution upon doping the Mott/charge transfer insulator; the theoretically microscopic study of this question is indeed very challenging and under much debate. In this work, however, we can look from the phenomenological aspects and experimental measurements. Regardless of the microscopic origin, in term of electronic compressibility, it is obvious that the system with slower chemical potential shifting upon carrier doping exhibits great capability in electronic compressibility. With this slower chemical potential shifting, the host can store more charge carrier while maintaining the potential; this suggests implication on energy storage applications.

In this study, we will demonstrate the fundamental reason relied on Mott gap closing to imply the selection criteria for the good candidate of battery electrode based on the literature report data of the electrochemical measurement of Cu, Mn, Co and Fe based electrode. As nickel oxide (NiO) can be the representative of Mott-Hubbard picture, we select NiO as a case study for examining the evolution of chemical potential in doped classic Mott-insulator by using Angle-resolved photoemission spectroscopy technique.

1.2 Research objectives

1.2.1 To experimentally investigate the electronic structure evolution of the classic Mott-insulator NiO by photoemission spectroscopy.

1.2.2 To investigate the charge storage performance of Cu, Mn, Co and Fe based electrodes based on the reported research data.

1.2.3 To give the visualization of chemical potential shifting scenario of doped Mott-insulator for providing the supporting reason on the charge storage capability of battery electrode.

1.3 Outline of thesis

This thesis is divided into five chapters. In chapter I, the motivation on doped Mott-insulator and thesis objective are provided. In chapter II, we will present the experimental observation on chemical potential shifting on doped strongly correlated materials. The fundamental background of photoelectric effect and the Angle-resolved spectroscopy (ARPES) is described. Then, the details of energy storage and electrochemical measurements including cyclic voltammetry (CV) and Galvano static charge-discharge (GCD) are presented. After that, the general background on the electronic structure of NiO and the experimental observation is given. In chapter III, we provide the details of ARPES study on the electronic structure of the classic Mott-insulator NiO. The DFT-calculation is also provided. In chapter IV, we present experimental ARPES results and describe how to process the results and illustrate the electronic structure evolution of NiO upon electron doping. In chapter V, the charge storage capacity of the Cu, Mn, Co, and Fe based batter electrodes will be determined based on the reported research data on the discharge profile. We will make the discussion and give the visualization of the chemical potential shifting scenario on the doped strongly correlated materials. In chapter VI, the conclusion and future direction are described.

CHAPTER II

LITERATURE REVIEWS

This chapter begins with the fundamental description in Mott-insulator and the background of the NiO (strongly-correlated materials, typically charge transfer insulator) in the view point of electronic structure. Then, the observation on chemical potential shifting in doped strongly correlated materials is described. After that, the fundamental background of the photoelectric effect is given, followed by “Angle-resolved photoemission spectroscopy” which is the synchrotron technique for exploring the electronic structure of material. Since the scope of interest relates to the energy storage application, the energy storage and electrochemical measurements on electrode materials are provided.

2.1 Mott insulator

The Mott insulator describes a class of material with a partially filled electronic band, however; it fails to conduct electricity despite having mobile charge carriers. This insulating behavior is not due to a lack of available electronic states but arises from strong electron-electron interactions that hinder charge transport. In other words, Mott insulator is a fascinating state of matter that arises from strong electronic correlations and represents a departure from conventional band insulators. Understanding the Mott insulator represents a crucial step toward unraveling the complex interplay between electronic correlations and emergent phenomena. The Mott insulating state is often described within the framework of the Hubbard model, a simple and powerful theoretical construction that incorporates both electron hopping and Coulomb repulsion.

The Mott transition, which separates the Mott insulating state from a metallic state, is a quantum phase transition driven by varying the strength of electron-electron interactions or the electron filling. At the transition point, the system undergoes a dramatic change in electronic properties, leading to the emergence of novel phenomena, such as metal-insulator transitions, charge ordering, and magnetism. The nature of the Mott transition remains an active area of research, with theoretical and experimental efforts aimed at unraveling its intricate details. Doped Mott insulators give a fascinating class of materials that exhibit a range of intriguing

phenomena arising from the interplay between strong electron-electron interactions and charge carrier doping and alters the electronic and magnetic properties of the parent Mott insulating state. In addition, these materials give us to explore the effects of doping on electronic correlations, phase transitions, and the emergence of novel quantum phases. Understanding doped Mott insulators is of great importance for both fundamental physics and technological applications.

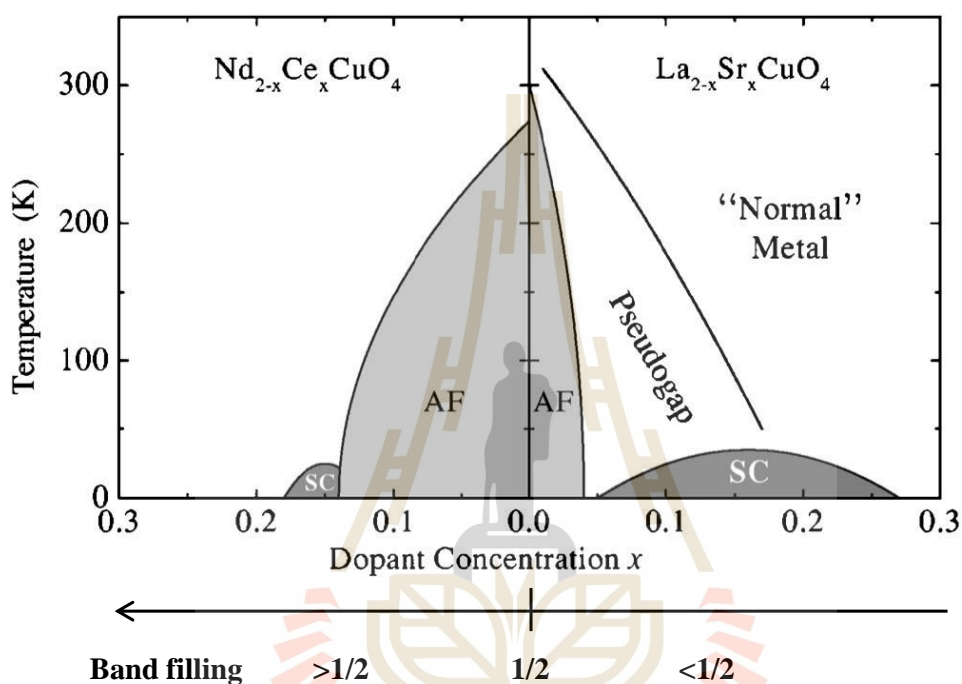


Figure 2.1 Schematic phase diagram of high- T_c superconductors presents hole doping LSCO (right) and electron doping NCCO (left) (Lee et al., 2006).

Historically, the discovery of the high T_c superconducting materials has gain the interest in the electronic structure of the late-transition-metal oxides. Specifically, the parent compounds of high T_c are known to be Mott-insulator. One of the most famous is the high T_c cuprate superconductors. They share the common feature of square planar copper-oxygen-layers separated by charge reservoir layers. The undoped materials are antiferromagnetic Mott-insulator. By substituting Sr for La in La_2CuO_4 , the introduction of holes into the CuO_2 plane occurs. As a result, there is a significant decrease in the Néel temperature, and at a higher level of hole doping, the material transitions into a superconducting state. This is the so called “214” or LSCO system of the type $\text{La}_{2-x}\text{Sr}_x\text{Cu}_2\text{O}_4$ with T_c around 40K. While hole doping is prevalent in most high T_c superconductors, there exists a small subset of compounds that can be electron-doped. One notable example is $\text{Nd}_{2-x}\text{Ce}_x\text{CuO}_4$

(NCCO), which has been extensively studied. In general, compounds in this material class have the chemical formula $R_{2-x}M_xCuO_4$, where the rare-earth element (R) is substituted with Pr, Nd, Sm, or Eu, and M can be either Ce or Th. Investigating superconductivity in strongly correlated systems necessitates many experimental techniques. Angle-resolved photoemission spectroscopy (ARPES), scanning tunneling microscopy (STM), neutron scattering, and transport measurements provide valuable insights into the electronic structure, pairing mechanism, and collective excitations. Spectroscopic tools, such as Raman spectroscopy and optical conductivity measurements, also offer valuable information about the superconducting gap structure and the interplay of charge, spin, and lattice degrees of freedom. The theoretical description of superconductivity in strongly correlated systems is a formidable task. Numerous theoretical frameworks, including the Hubbard model, t-J model, and extended Hubbard models, have been employed to capture the underlying physics. However, a comprehensive theoretical understanding of high-temperature superconductivity is still elusive.

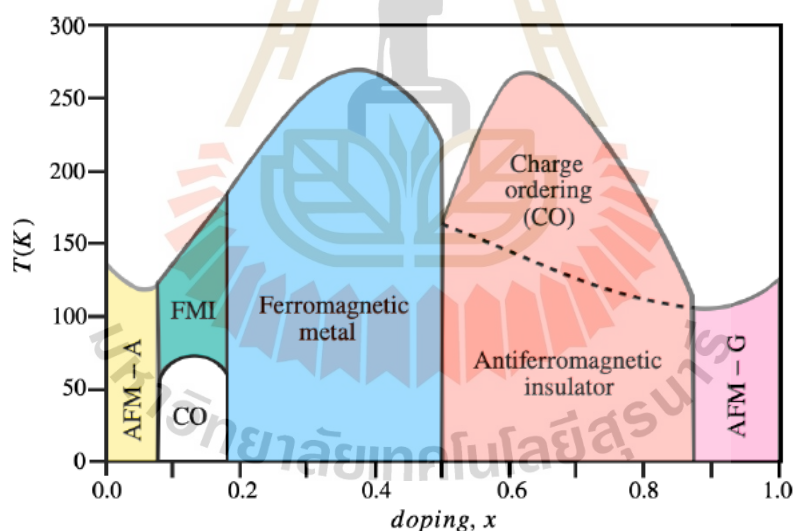


Figure 2.2 Schematic phase diagram of $La_{1-x}Ca_xMnO_3$.

Another fascinating property exhibited by doped Mott-insulator is colossal magnetoresistance (CMR). It refers to a significant change in electrical resistance in the presence of an external magnetic field, observed in certain manganite materials. The phenomenon arises from the interplay between charge, spin, and orbital degrees of freedom, and has attracted widespread interest due to its potential applications in spintronics and magnetic sensing. Doped manganites $R_{1-x}A_xMnO_3$ (where R^{3+} is a rare

earth such as La, Pr, etc. and A^{2+} is usually Ca or Sr) with the perovskite structure attract considerable attention. They show an astonishing variety of different types of ordering: orbital, magnetic, charge ordering. These systems have very complicated and rich phase diagrams. For example, undoped LaMnO_3 is a perovskite with localized electrons, and an antiferromagnetic Mott-insulator; its Mn^{3+} ions have configuration $t_{2g}^3 e_g^1$. When La^{3+} is replaced by Sr^{2+} or Ca^{2+} , some e_g -electrons are removed or the system is doped with e_g holes. As the doping level is increased in this system, experimental observations reveal a series of transitions, as depicted in Figure 2.2. It exhibits insulating phases with different types of magnetic ordering. The most interesting is the phase existing in the range $0.2 < x < 0.5$, which is a ferromagnetic metal. It was during this phase that the remarkable phenomenon of strong resistivity suppression by a magnetic field was discovered.

Understanding the mechanism of complex phenomena in doped Mott-insulators is a major challenge for researchers and is still debated. In this study, rather than trying to understand the deep details in the mechanism of doped Mott-insulators, we would like to scope on study application in energy storage based on the doped-Mott insulator.

2.2 Nickel Oxide (NiO)

Nickel oxide (NiO) is a compound consisting of nickel and oxygen atoms, belonging to the class of transition metal oxides. The NiO possesses rock salt crystal structure as shown in Figure 2.3. The Ni^{2+} is bonded to six equivalent O^{2-} atoms to form a mixture of corner and edge-sharing NiO_6 octahedra. It has attracted significant attention in various scientific and technological fields due to its unique properties and potential applications. Specifically, NiO has shown potential in energy storage applications such as lithium-ion batteries and supercapacitors due to its high theoretical capacity, good cyclability, and low cost. In the field of catalysis, NiO-based catalysts have been widely studied for various catalytic reactions. The tunable properties of NiO, such as surface area, morphology, and doping, allow for enhanced catalytic activity and selectivity. In the scope of sensors, NiO-based gas sensors have been developed for the detection of toxic gases, such as carbon monoxide, nitrogen oxides, and volatile organic compounds. The sensitivity and selectivity of NiO sensors can be improved by controlling the morphology, doping, and operating temperature. In Optoelectronics, NiO finds applications in transparent conductive coatings, solar cells, and electrochromic devices due to its wide bandgap and electrical conductivity control through doping.

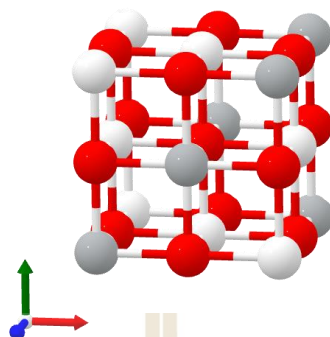


Figure 2.3 The typical rock salt structure of NiO (red and white color represent Ni and O atom, respectively).

Fundamentally, Nickel oxide has a Ni $3d^8$ O $2p^6$ outermost electronic configuration and has available room for two more electrons in 3d orbital. This partially filled d band suggests that these materials should be metals. However, it was found that NiO is an insulator with large energy gap. The reason is that the on-site Coulomb repulsion between the electrons within the 3d orbitals prevents them from moving freely, resulting in localized electron states. This localization of electrons and the associated Mott-Hubbard gap leads to an insulating state in NiO. It is an antiferromagnetic material with a Néel temperature around 523 K, above which it becomes paramagnetic. NiO is optically transparent in the visible range and exhibits a wide bandgap making it useful for optoelectronic applications. It also demonstrates high electrical resistivity, thermal stability, and chemical inertness, which make it suitable for various catalytic, sensor, and energy storage applications.

The electronic structure of NiO was experimentally explored by the x-ray photoemission spectroscopy (XPS), bremsstrahlung isochromat spectroscopy (BIS) (Sawatzky et al., 1984). The identification of the peak in Mott-Hubbard model can be theoretically investigated by local cluster theory (Fujimori et al., 1984). The complete of valence and conduction band of NiO can be displayed as Figure 2.5. The experimental results show that NiO is the insulating state with the band gap 4.3 eV (Fujimori et al., 1984). The strong Ni d-d coulomb interaction (d^7 to d^9 states in Mott-Hubbard picture) is between 7 and 9 eV. In addition, it is obvious that the O 2p hole state (d^8L) locate inside the d-d correlation gap. In this scenario, the NiO is regarded as the strongly correlated material in the type of charge transfer insulator

(technically, the onsite coulomb (U) greater than charge transfer energy (Δ)) as can be illustrated in Figure 2.6.

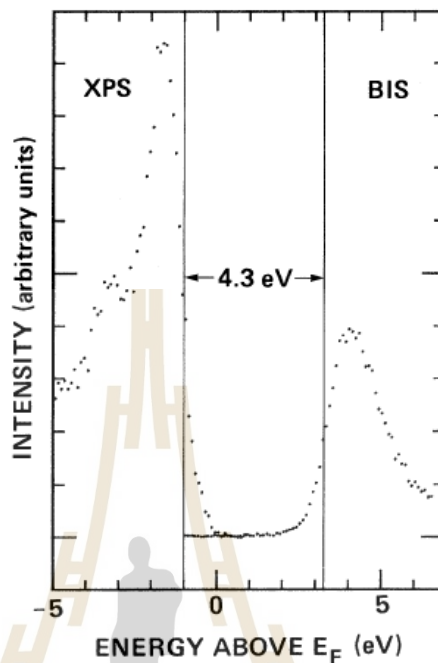


Figure 2.4 XPS and BIS spectra of NiO presenting the 4.3 eV band gap (Sawatzky et al., 1984).

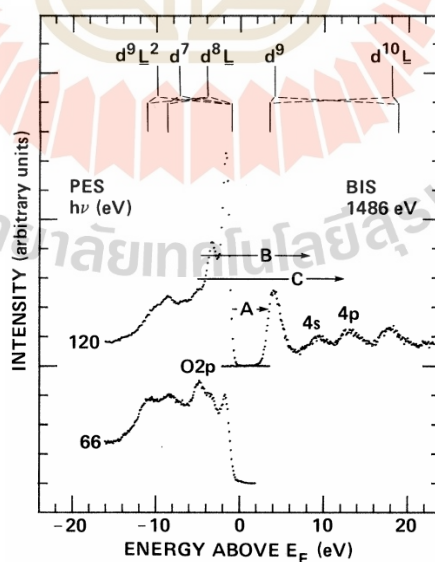


Figure 2.5 Electronic structure of NiO observed by XPS and BIS and assigned states in the Mott-Hubbard Picture (Sawatzky et al., 1984).

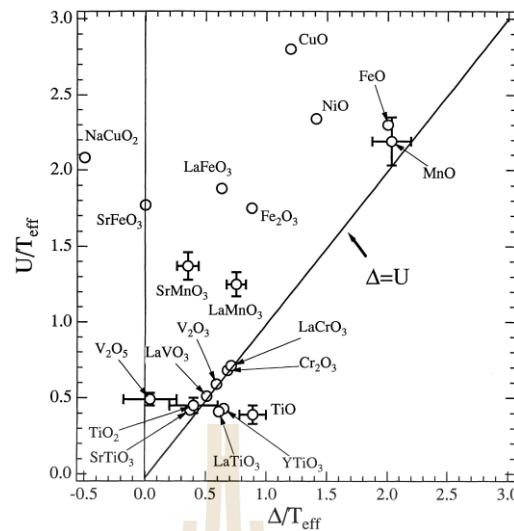


Figure 2.6 Zaanen–Sawatzky–Allen U - Δ plot for transition-metal oxides. The given compounds are classified either in the Mott–Hubbard in the regime ($\Delta > U$) or in the charge-transfer regime ($U > \Delta$) (Fujimori et al., 2002).

2.3 Chemical potential shift

Chemical potential is a fundamental concept in thermodynamics and statistical mechanics that quantifies the energy change in a system as a result of adding or removing particles. On other words, this parameter refers to capability to charge compressibility in the system by $\kappa_e = (1/n^2)(dn/d\mu)$, where κ_e is charge compressibility, n is the carrier density, and μ is the chemical potential. In the field of high T_c superconductor, the chemical potential changing is experimentally measured to describe the dynamic or evolution of electronic structure of material upon electron/hole doing in high T_c parent compounds. Conventionally, the chemical potential shifting can be determined by three ways (Wen et al., 2020):

- Measure core level shifting (XPS-technique)
- Deep valence band shift (UPS-technique)
- Measure Work function

In this review, we would like to concentrate on the chemical potential changing in doped strongly correlated materials. The aim is to illustrate possible scenario of chemical potential evolution in doped strongly correlated materials.

2.3.1 Chemical potential pinning

Since the vast majority of high- T_c cuprate superconductors are hole-doped Mott-insulator, there are extensive experimental study performed on this kind

of compound. One of the outstanding issues is that how the chemical potential evolves upon doping. In 1997, Ino et al., have been experimentally studied the chemical potential shift in correlated electron system by photoemission spectroscopy (PES). In his work, the chemical potential shift ($\Delta\mu$) in $\text{La}_{2-x}\text{Sr}_x\text{CuO}_4$ (LSCO) upon hole doping was measured via core level photoemission spectroscopy. The graph of $\Delta\mu$ in LSCO as function of hole-carrier concentration is plotted in Figure 2.7. The experimental results showed two distinguish features in the chemical potential evolution in LSCO upon hole doping. In over doping region ($x > 0.15$), the chemical potential move downward to the higher binding energy resulting in the negative in the chemical potential shifting ($\Delta\mu$) which is the commonly expected result in the hole doping. On the other hand, for the doping regime in between under dope to optimally dope regime ($x < 0.15$), it has been found that the chemical potential remain near the same energy level, thus the chemical potential shift is suppressed. In addition, the chemical potential pinning have also experimentally found in hole doped $\text{La}_{2-x}\text{Sr}_x\text{NiO}_4$ (LSNO) by the core level photoemission investigation (Satake et al., 2000). It is noted that the surprisingly feature of chemical potential pinning is most likely related to the inhomogeneous of charge distribution in microscopic scale or the formation of stripes.

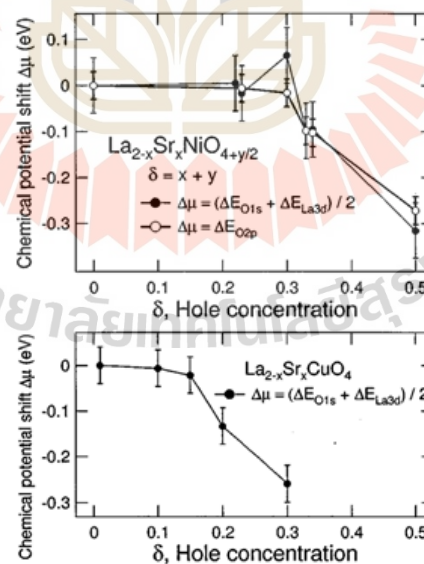


Figure 2.7 Chemical Potential Shift in hole doped LSCO and LSNO (Satake et al., 2000).

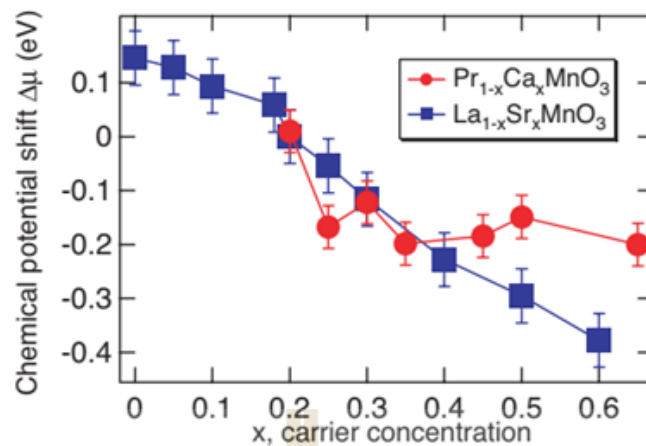


Figure 2.8 Chemical Potential Pinning in PCMO (Ebata et al., 2008).

Doped perovskite-type manganites $R_{1-x}A_xMnO_3$ have been attractive to be experimentally investigated according to remarkable phenomena in particular colossal magnetoresistance (CMR). They exhibit very complicated and rich phase diagram due to the variety of orbital, magnetic and charge ordering. In addition, there is a report that the bandwidth of manganite compound is the key parameter that control physical properties of the manganites.

Mostly, the shift of chemical potential of strongly correlated system is studied as a function of doping concentration. The effect of hole-concentration and bandwidth on chemical potential shift in manganite compound has been experimentally investigated by PES technique (Ebata et al., 2008). The illustration of chemical potential shift in $La_{1-x}Sr_xMnO_3$ (LSMO) and $Pr_{1-x}Ca_xMnO_3$ (PCMO) is presented in Figure 2.8. In $La_{1-x}Sr_xMnO_3$ (LSMO), the system with the widest bandwidth among the manganites, the chemical potential shift deduced from photoemission spectra displays a monotonous shift without indication of chemical potential pinning. The author points out that stripe effects are negligibly weak in the LSMO (large-bandwidth systems without charge-ordering region). In case of the $Pr_{1-x}Ca_xMnO_3$ (PCMO), the system with small bandwidth, A clear downward chemical potential shift with hole concentration is observed for $x < 0.25$ which is analogy to the case of LSMO. However, there is surprisingly a suppression in chemical potential shift observed in PCMO in the region $x > 0.3$. The pinning of chemical potential in PCMO is attributed to a particularly charge-ordered state over the wide hole concentration region between $x = 0.3$ and $x = 0.75$ in electronic phase diagram.

2.3.2 Negative Electronic Compressibility (NEC)

The electronic structure generally remains rigid against carrier doping. Add more electrons filling will make chemical potential increasing (positive electronic compressibility, PEC). On the other hand, it is discovered that the chemical potential can be decreased upon increasing electron concentration. This phenomenon can be specifically referred as the negative electronic compressibility (NEC). The experimental evidence from Angle-resolved photoemission spectroscopy on Doped correlated materials ($\text{Sr}_{1-x}\text{La}_x$) Ir_2O_7 obviously illustrates that the decreasing in chemical potential occurs as increase electron doping concentration (He et al., 2015). Figure 2.9 illustrate the relatively movement of the valence band maximum (VBM) and conduction band minimum (CBM) of ($\text{Sr}_{1-x}\text{La}_x$) Ir_2O_7 as increasing in electron doping. Such a band gap deduction or Mott-gap closing yields to the negative sign of $\Delta\mu/\Delta n$ or NEC. This finding confirms a breakdown of rigid band picture to describe scientific observation. On other words, it can be generalized that increasing in doping concentration will weaken the interaction yielding to the reduction of correlation gap.

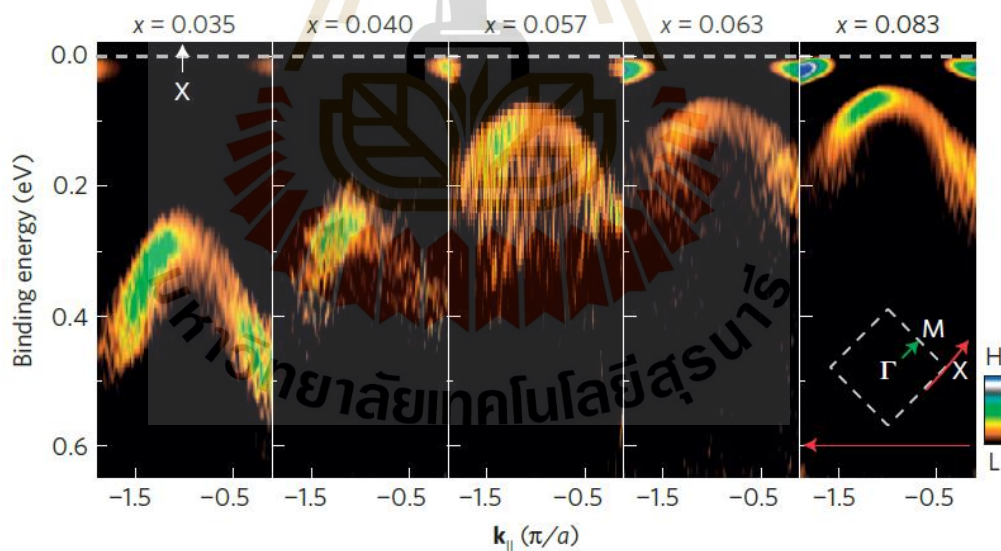


Figure 2.9 The electronic structure evolution on electron doping in strongly correlated ($\text{Sr}_{1-x}\text{La}_x$) Ir_2O_7 . As electron doping increases from $x = 0.035$ to $x = 0.083$, the valence band top moves upward, while the conduction band bottom moves downward resulting in effective lowering of $\Delta\mu$ in the NEC scenario (Hu et al., 2015).

2.4 Photoelectric Effect

The photoelectric effect, first discovered by Heinrich Hertz and further elucidated by Albert Einstein in 1905, refers to the ejection of electrons from a material's surface upon exposure to electromagnetic radiation, typically light. This phenomenon challenged classical wave theories and paved the way for the development of quantum mechanics, revolutionizing our understanding of the nature of light and the behavior of matter.

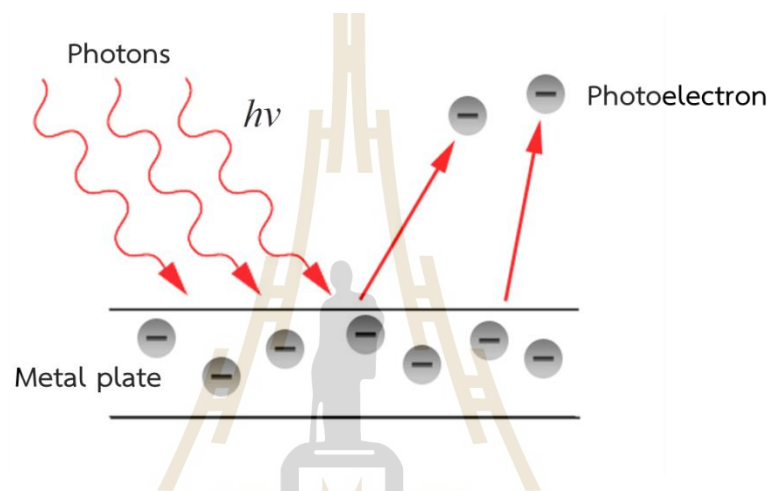


Figure 2.10 Photoelectric phenomena for simple explanation.

The photoelectric effect experiment conducted by Hertz involved irradiating a metal surface with various frequencies of light and measuring the resulting electron emission. The simplified photoelectric effect can be visualized as presented in Figure 2.10. Key observations included the dependence of electron kinetic energy on the frequency (not intensity) of incident light and the existence of a threshold frequency below which no electrons were emitted, regardless of light intensity. The photoelectric effect provided strong evidence for the particle-like behavior of light, challenging the wave theory of electromagnetic radiation. Einstein's explanation introduced the concept of photons, discrete quanta of light energy, with each photon having energy proportional to its frequency, as given by $E = h\nu$, where E represents energy, h is Planck's constant, and ν denotes frequency.

The work function (ϕ) characterizes the minimum energy required to liberate an electron from a material's surface. Electrons can only be emitted when the energy of a photon exceeds the work function. The threshold frequency corresponding to the minimum frequency for electron emission is determined by the

ratio of ϕ/h .

The photoelectric effect obeys the principles of energy and momentum conservation. The energy of the incident photon is used to overcome the work function and impart kinetic energy to the emitted electron. The momentum of the photon is transferred to the electron. The photoelectric effect shattered the classical wave theory's limitations and played a crucial role in the development of quantum mechanics. It demonstrated the particle-wave duality of light and established the quantization of energy.

2.5 Angle Resolved Photoemission Spectroscopy (ARPES)

ARPES is an experimental synchrotron technique based on photoelectric effect. The microscopic of photoelectric effect is simply can be explained with the concept of photon (particle of light). When the light is incident on the sample, electron will absorb the photon and escapes out of the sample surface (if the energy of absorbed photon is greater than work function of materials). In a typical ARPES measurement, a sample is placed under ultrahigh vacuum condition. Experimentally, the synchrotron light shine on to the sample and the photo emitted electrons (photoelectrons) are then collected and analyzed with respect to their kinetic energy and emission angle by electron analyzer. According to the conservation of energy, the binding energy of electron (E_B , the smallest energy required to remove electron from the sample surface) can be determined by following relation:

$$E_B = h\nu - E_{kin} - \phi \quad (1)$$

Where, $h\nu$ is photon energy, E_{kin} is the kinetic energy of photoelectron, and ϕ is the work-function (energy required for an electron at fermi level to escape to the vacuum level). Alternatively, the measured electron binding energy directly represents the depth of the energy level of photoelectrons inside the sample.

In term of the momentum space, the in-plane momentum k_{\parallel} (parallel component with respect to sample surface) of photoelectron is conserved throughout the photoemission process. Under the emission angle (θ), the in-plane momentum k_{\parallel} can be derived the following equation:

$$k_{\parallel} = \sqrt{\frac{2m_e E_{kin}}{\hbar^2}} \sin \theta \quad (2)$$

The basic experimental ARPES measurement can be explained by the illustration as presented in Figure 2.11.

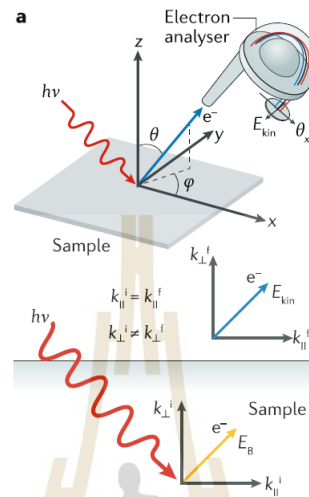


Figure 2.11 The fundamental principle of Angle-resolved photoemission spectroscopy (ARPES) measurement. The top panel illustrates the geometry of ARPES measurement. As the photon (red line) incident into sample, the electrons are ejected from the sample surface (blue line) and collected by electron analyser. The bottom panel presents the momentum conservation of electrons. The in-plane momentum (k_{\parallel}) is conserved, while the perpendicular to the surface is not conserved (Baiqing Lv et al., 2019).

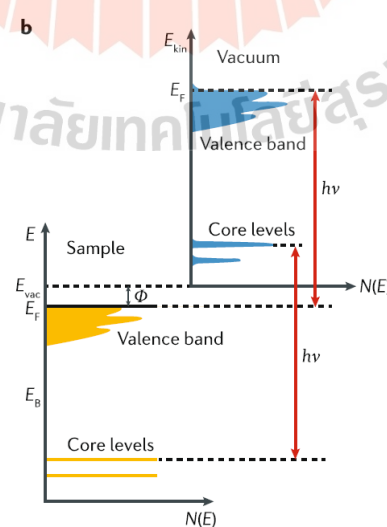


Figure 2.12 A schematic of energy level of photoelectron in ARPES measurement. The energy is conserved associated with equation (1) (Baiqing Lv et al., 2019).

The photoemission process is frequently discussed within the context of the three-step model: photon absorption, electron transport to the surface, and emission of the electron into the vacuum (Sobota et al., 2021):

(1) The photon drives a direct optical transition for an electron in the bulk of the material: as a photon interacts with a material, it can excite an electron from its initial state to a higher energy state. This process is known as an optical transition. This step contains the information on the intrinsic electronic structure of the material.

(2) The electron propagates to the surface: after the optical transition, the excited electron may undergo various scattering processes as it moves through the material. These scattering processes can be both elastic (where the electron retains its energy) or inelastic (where the electron loses or gains energy through interactions with other particles or lattice vibrations). These scattering processes impose an effective mean free path on the electron, which represents the average distance it can travel before being scattered.

(3) The electron is transmitted through the surface barrier: Eventually, the electron reaches the surface of the material. At the surface, it can tunnel through this surface barrier and transition into a free-electron plane wave state in the vacuum. The electron's behavior in the vacuum can then be described by free electron plane wave state. This free-electron state allows the electron to travel towards a detector or undergo further interactions and measurements.

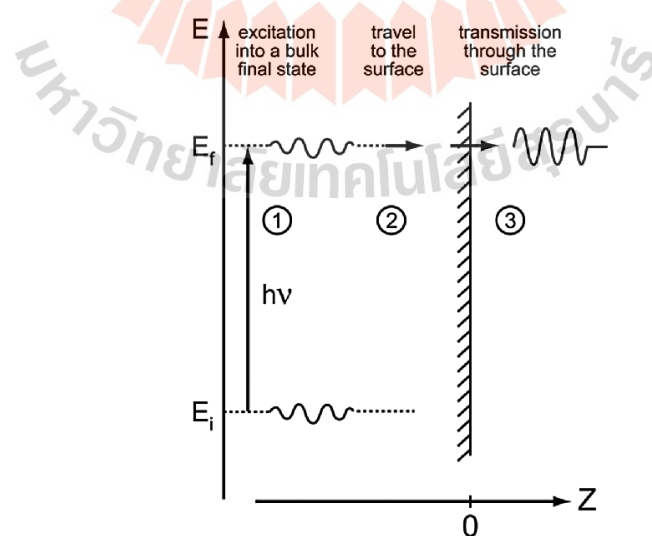


Figure 2.13 The Illustration of three-step crucially used for describing the possible photoemission process.

The ARPES technique is known for its exceptional sensitivity to surface properties. It requires the sample to have a clean and well-ordered flat surface. To ensure cleanliness and prevent surface contamination, a single crystal is typically cleaved in situ and measured under conditions of ultrahigh vacuum. Another method used to achieve an atomically clean and flat surface is the polish-sputter-anneal technique. This involves polishing the sample, subjecting it to repeated sputtering, and then annealing it. This approach is suitable for materials with strong chemical bonding, as the surface can be crystallized through annealing in a vacuum environment.

The light source is the crucial factor for the ARPES measurement since the photon energy determines the photoelectron escape depth. In addition, photon energy also impacts the range and resolution of the momentum space determination (Sobota et al., 2021). In practice, high photon energy is often preferred for its ability to provide extensive energy-momentum coverage. Synchrotron light sources, with their tunable energy range spanning from ultraviolet (UV) to hard X-ray wavelengths, are commonly used due to their versatility. Laser light sources, on the other hand, offer lower photon energy but provide higher flux, resulting in improved momentum resolution. Additionally, gas discharge lamps offer a laboratory-based option for ARPES measurements, although there are some limitations related to beam size and polarization. A summary of each light source is presented below.

1) Synchrotron light source

- Photon energy adjustable (continuously and easily tunable by adjusting the undulator and monochromator)
- The polarization-dependent measurement accessible (enable to identify the orbital character of bands)
- Spot size of $10 \sim 100 \mu\text{m}$

2) Laser source

- Exceptionally high intensity of photons
- Remarkable consistency and stability in terms of energy
- Small spot sizes $< 5 \mu\text{m}$

3) Gas discharge lamp

- commercially available (suitable for laboratories)
- Most common are He I α (21.22 eV), He II α (40.81 eV), Ne I α (16.85 eV), and Ar I (11.62 eV) emission
- Typical spot sizes $\sim 1 \text{ mm}$

2.6 Energy Storage

In the past decades, traditional non-renewable energy supplies (e.g., coals, oil, and natural gas) have been overused to meet the rapid increase of global energy demands. Nowadays, the exploration and research into renewable green energy technologies are increasing rapidly due to the urgent need for sustainable and environmentally friendly energy sources. To utilize these intermittent renewable energies efficiently, developing low-cost and high-performance electrical energy storage is extremely focused.

A battery is an energy storage device that facilitates the conversion of electrical energy into chemical energy and vice versa. It achieves this by transferring ions between two electrodes during charge and discharge processes as presented in 2.10. During the charging of a lithium-ion battery (LIB), electrons are extracted from the cathode particles, through conductive agents such as carbon black, current collector and the external circuit, and finally enter the anode particles. The electrochemical potential difference of lithium ions (Li^+) between the two electrodes provides the driving force for the migration of Li^+ from the cathode (positive electrode) to the anode (negative electrode) through the electrolyte. This movement helps maintain approximate bulk charge neutrality within the cathode and anode particles.

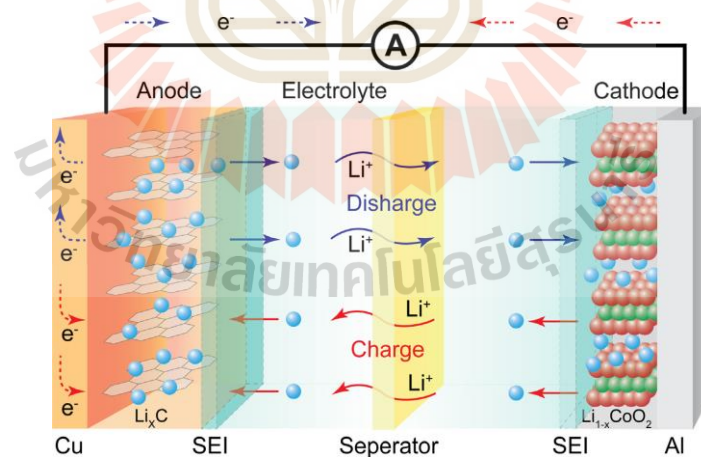


Figure 2.14 Schematic of Li-ion battery (LIB) consists of a negative electrode (graphite), positive electrode (LiCoO_2), current collectors, liquid electrolyte and separator. Li-ions move from the positive (negative) electrode to the negative (positive) electrode through the electrolyte during charging (discharging); while electrons simultaneously travel through an external circuit to ensure charge balance (Zhang et al., 2017).

During the discharging process, the chemical energy stored in the electrodes (the chemical potential difference of polarons/ion pairs or neutral 'Li atoms' in the cathode and anode) is converted into electrical energy to power external devices or loads.

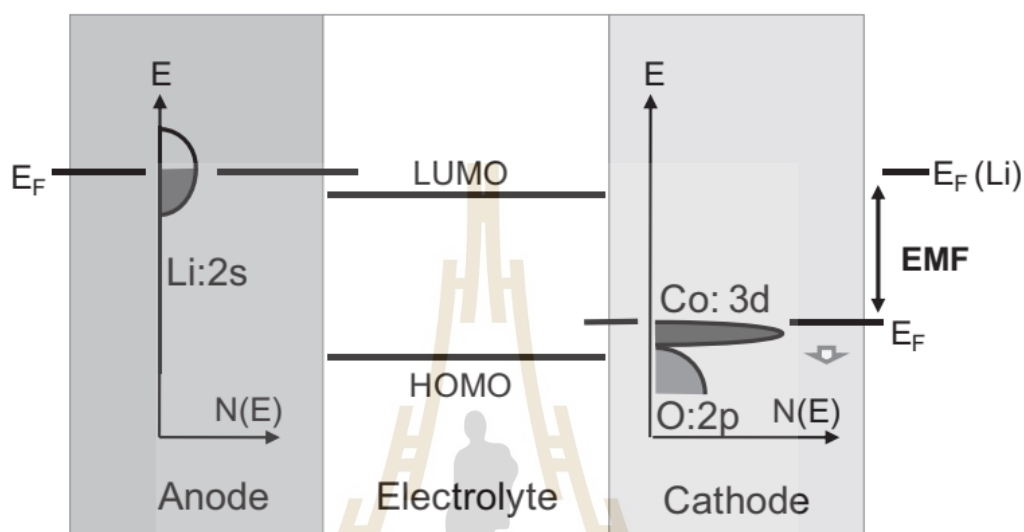


Figure 2.15 Schematic energy level in Li-ion Battery (Hausbrand et al., 2015).

Fundamentally, the energy levels of the battery components, including the cathode, anode, and electrolyte, can be represented diagrammatically as shown in Figure 2.15. This diagram traditionally illustrates the Fermi level of the electrode (or redox level) relative to that of lithium Li/L^+ . Specifically, the Fermi level of the anode is higher than that of the cathode, indicating that the work function of the anode is smaller compared to that of the cathode. The difference in the work function of these two components will define the realistic voltage of battery. In order to quantify the performance of electrode material, there is a tremendous study on both the active voltage region and the capacity of electrodes. The capacity and electrochemical reduction potential for a range of cathode and anode is illustrated in Figure 2.16.

In commercial LIBs, graphite is currently the most commonly used anode material. The incorporation of lithium into graphite occurs through an intercalation mechanism, where lithium ions are reversibly inserted into and extracted from the interlayer spaces of graphite during charge-discharge cycles. Specifically, the theoretical capacity of graphite is limited to 372 mAh g^{-1} due to the limitation of LiC_6 formation. Alternatively, conversion mechanisms involve electrode materials

undergoing conversion reactions to produce lithium oxide. Conversion anodes typically offer high specific and volumetric capacities, making them advantageous options. The cathodes are commonly made of transition metal compounds. In particular, layered LiCoO_2 is regarded as a novel cathode in Li-ion battery. The practical specific capacity of commercial LiCoO_2 (LCO) can reach around $140\text{--}165 \text{ mAh g}^{-1}$ at operating voltage 3 V. Spinel LiMn_2O_4 (LMO) also can be served as practical cathode (capacity around $100\text{--}120 \text{ mAh g}^{-1}$) with operating voltage 4 V. Besides, LiFePO_4 or LFP is also utilized as commercial cathode with a practical specific capacity of about $120\text{--}160 \text{ mAh g}^{-1}$ operated at 3.4 V. The indicators including cycle life, average working voltage, practical gravimetric capacity, safety, and cost, are fundamentally used to determine electrode materials, helping to find their proper applications. In this work, we are speculating if some of the good batteries associate with Mott/charge transfer insulator host materials.

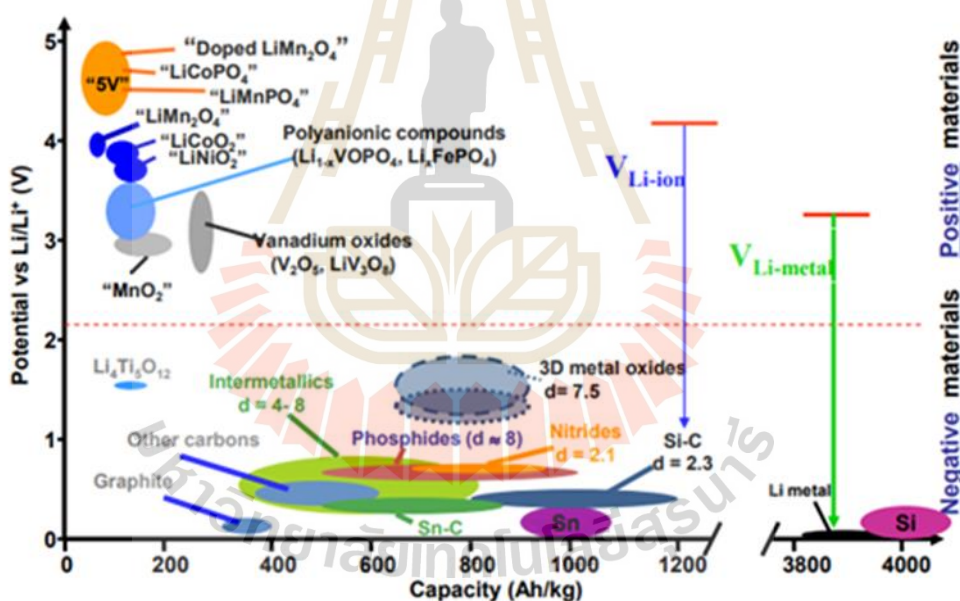


Figure 2.16 The operating potential and capacity of battery electrode (from <https://www.eai.in/blog/2018/12/research-status-of-anode/cathode-material.html>).

2.7 Electrochemical Measurements on Electrode Materials

The basic principles of electrochemical measurements and how to analyze electrochemical data in the battery research involve with Cyclic Voltammetry (CV) and Galvano static charge–discharge (GCD) testing techniques. The aim of battery testing is to estimate the energy/power density, conversion efficiency, and calendar lifespan. The determination of these features involves characteristic parameters such

as voltage, current, capacity, and testing duration. In the CV-technique, the current response at different applied voltage is determined (I-V curve). In the case of GCD, the voltage evolution under certain forced current (fixed-current) is investigated. Both of two-technique provide the information on the voltage and energy profiles of the tested battery electrode. In the following, the short description on electrochemistry concepts related to field of energy storage is given.

2.7.1 Cyclic Voltammetry (CV)

Cyclic voltammetry is an extensively used and effective electrochemical technique that allows for the study of electrode reduction and oxidation processes. In practice, it is necessary to determine the starting potential (E_1), final potential (E_2), and scan rate (v) for the experimental setup. The measurement involves applying a triangular voltage waveform to the electrochemical system, as illustrated in Figure 2.17. Figure 2.18 demonstrates a typical current response observed in batteries. By analyzing the data, the characteristic Gauss-type peak associated with a single electrode reaction can be observed, and the corresponding peak voltage and peak current can be determined.

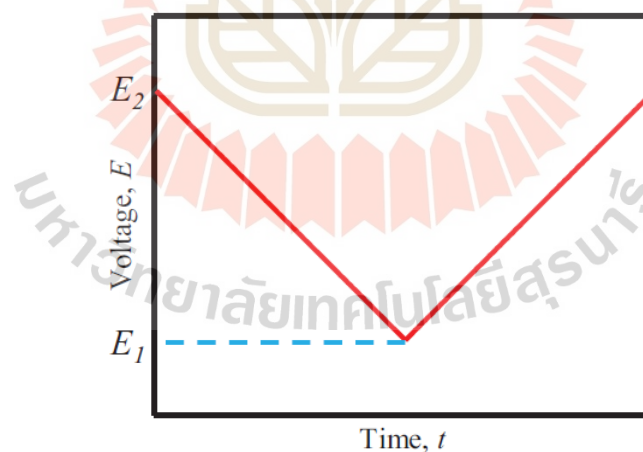


Figure 2.17 The voltage profile applied in CV measurement (Yang et al., 2019).

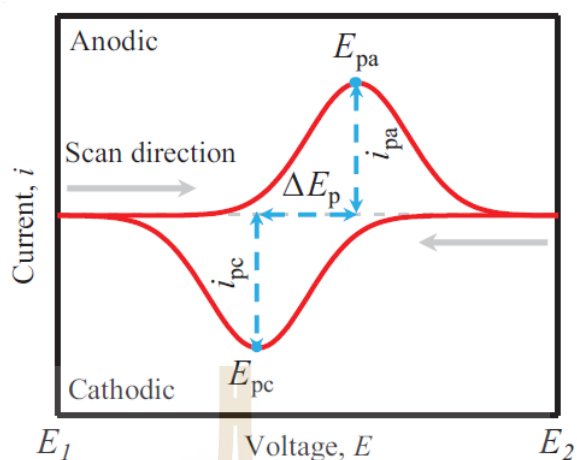


Figure 2.18 Current response versus voltage curves in CV measurement (Yang et al., 2019)

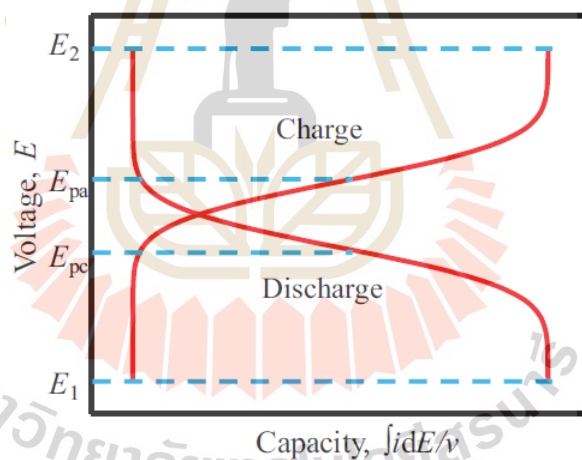


Figure 2.19 The voltage versus integral current curves in CV measurement (Yang et al., 2019).

To provide extensive explanation, the comparison of peak currents and the disparity in peak voltage between the anodic and cathodic reactions can be utilized to assess the reversibility of the electrochemical system. Furthermore, the cyclic voltammetry (CV) curves can be transformed into voltage versus capacity profiles, as shown in Figure 2.19, where the discharge and charge plateaus correspond to the cathodic and anodic peak voltages, respectively. Generally, when the y-axis represents specific current (measured in A g^{-1}) instead of current (A), integrating the area under the curve gives the specific capacity (in unit of mAh g^{-1}).

2.7.2 Galvano static charge–discharge (GCD)

The GCD (Galvanostatic Charge-Discharge) technique involves recording the voltage response while applying a constant current to the electrode. This method is widely used to assess the capacity, reversibility, stability, and rate capability of the electrode. In practice, it is necessary to determine the specific terminal voltage at which the current direction will reverse in order to initiate the GCD measurement. The charge and discharge processes, following the applied current profile illustrated in Figure 2.20, yield a voltage profile with a generally flat region, referred to as a plateau, as shown in Figure 2.21. Alternatively, the plateau region in the voltage profile can be analyzed using the differential capacitive curve (dQ/dV vs V) to visualize the presence of redox peaks, as demonstrated in Figure 2.22, which correspond to the plateau in the voltage profile. The voltage profile obtained from the GCD measurement (Figure 2.21) is equivalent to the voltage versus integral current curve derived from CV curves (Figure 2.19). Furthermore, the differential capacity curve (Figure 2.22) appears identically to the CV curves (Figure 2.18). In practical terms, the current is typically adjusted based on the mass of the active materials or the electrode area, depending on whether gravimetric or areal capacity is being determined. In the testing of half-cell batteries, the gravimetric capacity (measured in mAh g^{-1}) is commonly used, and the current is normalized to the specific current, expressed in units of A/g or C-rate current. Here, 1C is defined as the current required to fully charge or discharge the battery in one hour.

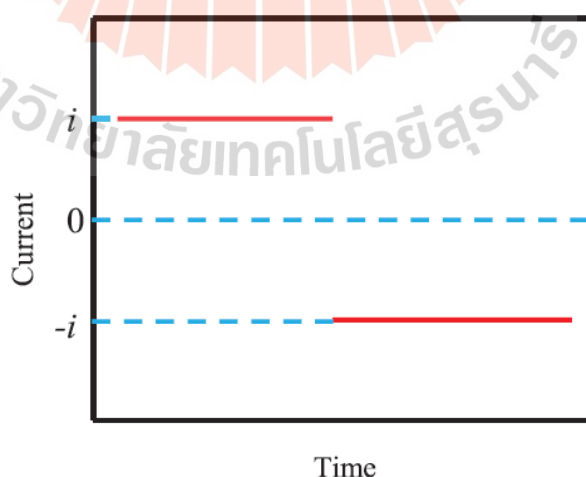


Figure 2.20 The current profile applied in GCD measurement (Yang et al., 2019).

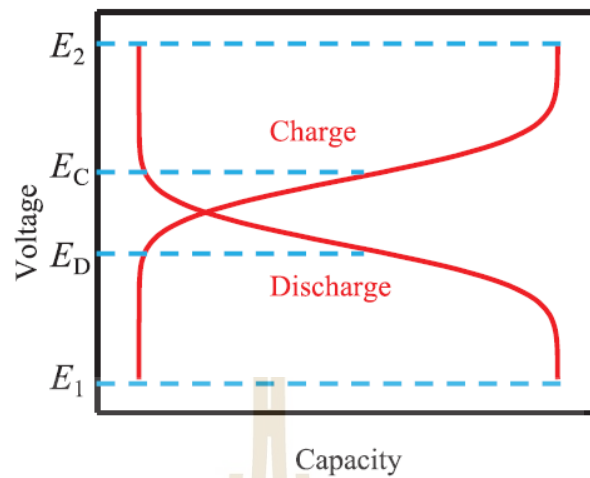


Figure 2.21 The typical voltage response versus capacity in GCD measurement (Yang et al., 2019).

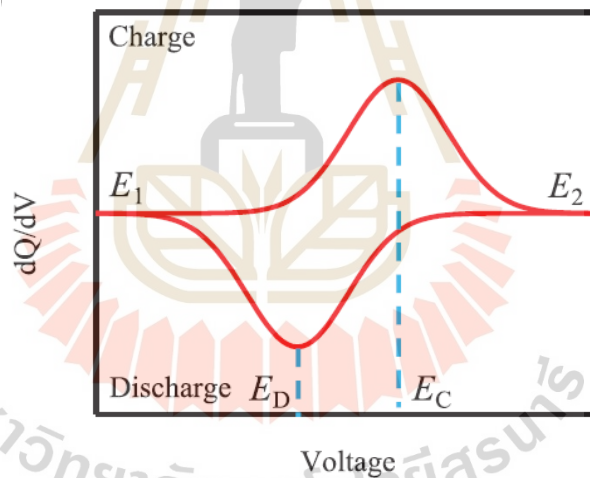


Figure 2.22 The differential capacity curve for charge and discharge in GCD measurement (Yang et al., 2019).

Regarding cycle stability, it can be assessed by repetitively performing charge and discharge cycles and determining the cycle number corresponding to an acceptable reversible capacity, often defined as 80% of the initial value, as shown in Figure 2.23. Lifespan is a critical parameter for rechargeable batteries, as a longer lifespan corresponds to a longer service time or lower time-averaged cost. The rate capability of an electrode can be evaluated by adjusting the current within an appropriate range. As the current rate is increased, the capacity tends to decrease due to increased polarization, as depicted in Figure 2.24. By analyzing voltage profiles

obtained at various current rates, the power and energy density can be calculated. The graph comparing energy density (Wh/kg) and power density (W/kg) shown in Figure 2.25 is frequently used to compare the energy-power characteristics of different power devices.

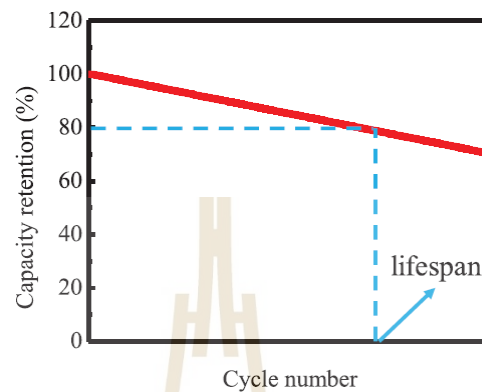


Figure 2.23 The typical cycle stability of battery electrode (Yang et al., 2019).

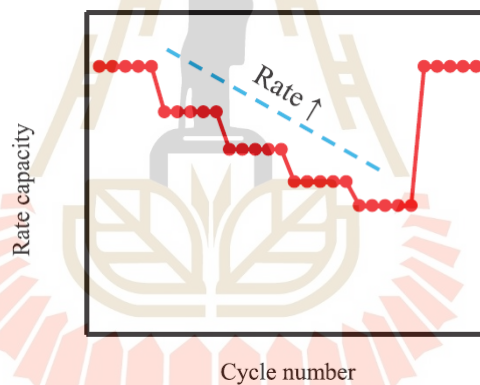


Figure 2.24 The rate capability performance (Yang et al., 2019).

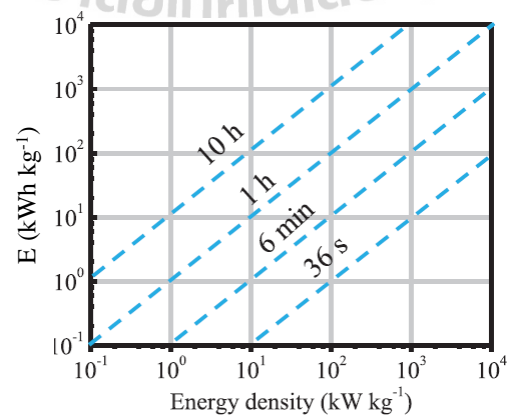


Figure 2.25 The Ragone diagram (Yang et al., 2019).

CHAPTER III
ANGLE-RESOLVED PHOTOEMISSION SPECTROSCOPY ON
STRONGLY CORRELATED MATERIAL:
THE CASE OF NICKEL OXIDE (NiO)

3.1 NiO sample

The NiO is strongly correlated material with the rocksalt crystal structure of as shown in Figure 3.1. The lattice constant of NiO is 4.19 \AA . In this study, NiO is selected as a case study of doped strongly correlated materials. Specifically, the commercial single crystal of Ni (100) produced by Crystalbase company is purchased and used as sample for experimental Angle-resolved photoemission spectroscopy (ARPES). In the sample preparation, the NiO sample with approximately $2.5 \times 2.5 \times 1 \text{ mm}^3$ in size was saw the edge with diamond saw to make it easy to enable surface cleaving. The sample was stuck by the conductive silver epoxy to the sample holder to make it more conductive as performing the measurement. Then, the top surface sample is connected with the top-post by the epoxy glue as shown by schematic in Figure 3.2. In the pre-measurement, the clean surface of NiO can be achieved by surface cleaving under the vacuum condition.

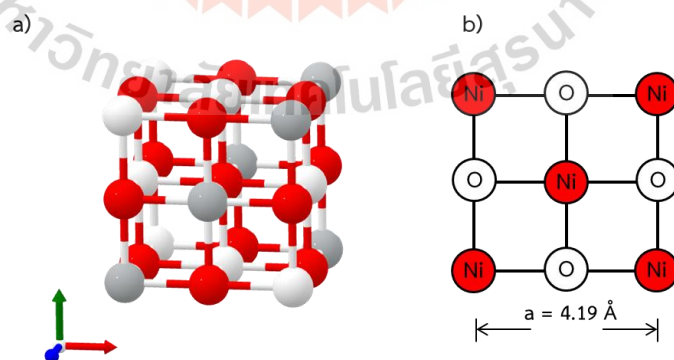


Figure 3.1 a) The crystal structure of NiO, the red and white color represent Nickel and Oxygen atom, respectively, b) The (100) plane of single crystal NiO with lattice constant 4.19 \AA .

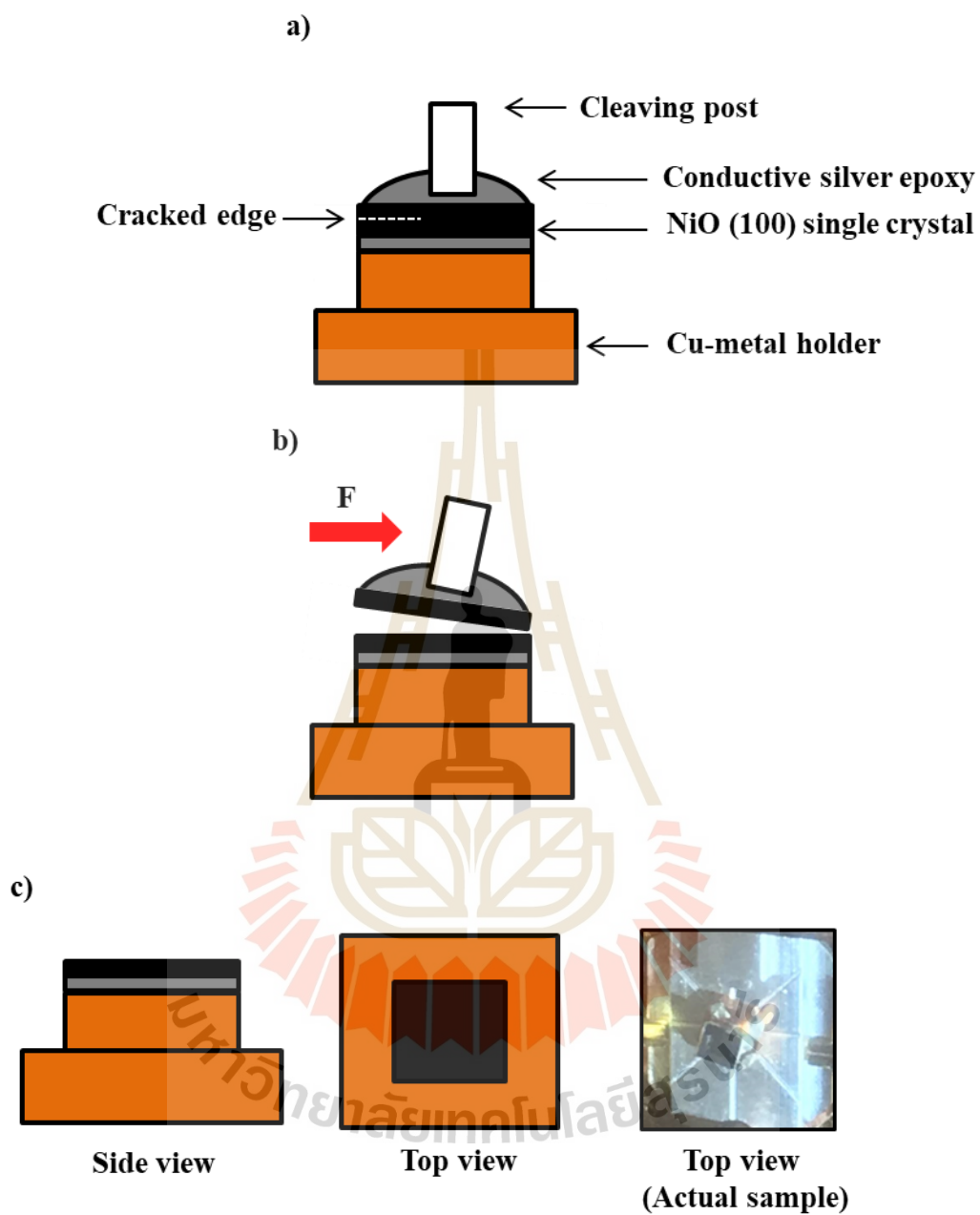


Figure 3.2 Schematic of a) NiO single crystal sample preparation for ARPES measurement consisting of the sample holder and cleaving post attachment, b) the surface cleaving associated by applied external force to the cleaving post under vacuum condition, c) the side view, top view, and the actual sample.

3.2 Experimental Angle-Resolved Photoemission Spectroscopy

The electronic structure of NiO was experimentally observed by angle-resolved photoemission spectroscopy (ARPES). The experimental study was held on experimental station 5-2, Stanford Synchrotron Radiation Light Source, USA. The photon energy was used at 60 eV and the measurement is conducted at the room-temperature under high vacuum condition. The base pressure is less than 5×10^{-11} Torr. The spot size of synchrotron source is $0.04(\text{H}) \times 0.01(\text{V}) \text{ mm}^2$ with the flux $\text{Flux} \sim 2 \times 10^{12}$ (ph/sec) and resolution $\Delta E/E \geq 2.5 \times 10^{-5}$. The measurement is performed with linear horizontal polarization. The analyzer detector is the SCIENTA DA30L electron analyzer. Firstly, the NiO sample is loaded into the prep chamber and then transferred into the main chamber for conducting the measurement. After that the fresh and clean surface of NiO is obtained by surface cleaving. Secondly, the ARPES-measurement is performed on the cleaved-surface NiO to explore the electronic structure of pure NiO sample. The experimental spectrum of pure NiO is collected and was presented as the undoped strongly correlated sample. Secondly, the alkaline metal evaporation on the cleaved NiO surface is performed to simulate in-situ surface electron doping. More specifically, the electron donating of alkaline metal on the surface of NiO sample gives us the transformation of undoped to electron-doped NiO. The electron doping is directly increased by the evaporation time. In this study, the specific evaporation time is at 20 and 40 s. Additionally, since the UV-shining is reported as the optional strategy to perform the in-situ surface electron doping, we also try to perform the UV-laser shining and perform the ARPES-measurement. The collected spectrum is analyzed and complementarily discussed with the alkaline metal evaporation strategy.

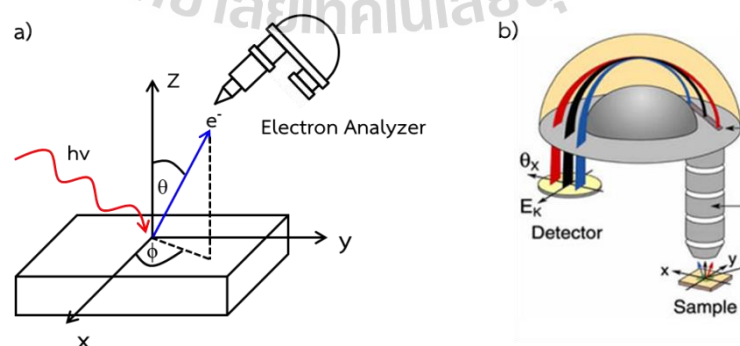


Figure 3.3 Schematic ARPES measurement: a) the photon (with energy $h\nu$) kicks the electron on the material surface out as the photoelectron and then collected by the

electron analyzer, b) the hemisphere electron bend the trajectories of electrons entering a narrow slit at one end and interpret the final radius as the kinetic energy.

3.3 Synchrotron Facilities

We would like to express our sincere gratitude to the collaborative synchrotron facilities that have played an instrumental role in enabling our research study. Their supported infrastructure has been vital in achieving our scientific goals. We acknowledge the following synchrotron facilities for their invaluable contributions:

- 1) Advanced Light Source (ALS), USA
- 2) Stanford Synchrotron Radiation Light Source (SSRL), USA
- 3) Shanghai Synchrotron Radiation Facility (SSRF), China
- 4) SOLEIL Synchrotron, France
- 5) Siam Synchrotron Light Source (SLRI), Thailand

Their advanced instrumentation and beamline access have allowed us to explore our research question, yielding crucial insights. We express our deepest appreciation for their contributions to our research.

3.4 Angle-Resolved Photoemission Spectroscopy Data

In the ARPES measurement, the electron analyzer records the intensities in angle and kinetic energy (the raw ARPES-spectra are corrected as the intensity in 2D pixels). The row of the table (y-axis) presents the kinetic energy (E_k) of photoelectron, while the column of the table (x-axis) denotes the emission angle (θ) or the momentum (k) in the specific direction. In pre-processing, the kinetic energy of photoelectron will be converted and present in term of binding energy (E_b) by equation (3.1). The fermi level (where binding energy is zero) is defined by calibrating with the metal gold sample. In the momentum-space conversion, the emission angle (θ) is mathematically converted into the momentum ($k_{//}$) by the formula in equation (3.2):

$$E_B = h\nu - E_{kin} - \phi \quad (3.1)$$

$$k_{//} = \sqrt{\frac{2m_e E_{kin}}{\hbar^2}} \sin \theta \quad (3.2)$$

The following illustration presents the raw data from the APES measurement of the graphite in the purpose of data visualization.

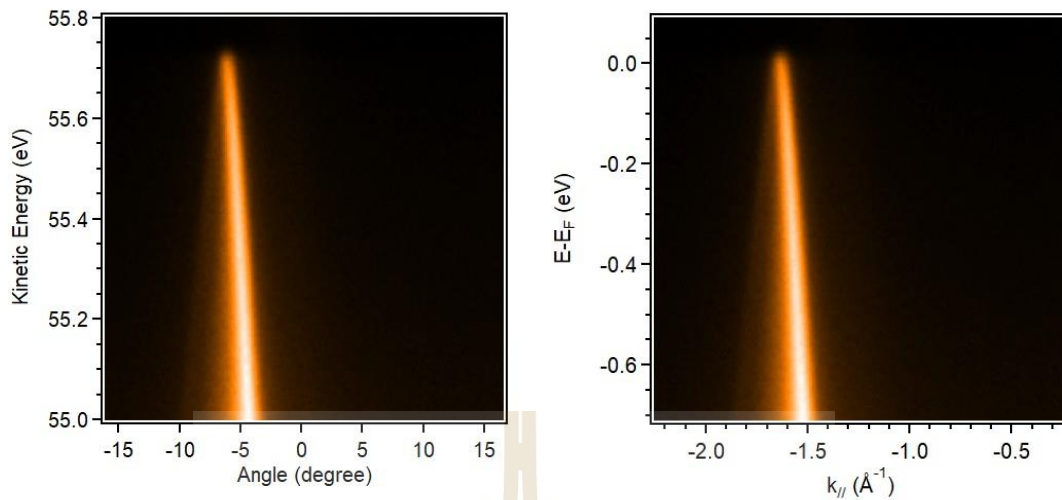


Figure 3.4 The raw ARPES-spectra of graphite: a) kinetic energy versus angle, and b) binding energy versus momentum space.

In the further analysis, the background subtraction needs to be considered to distinguish the intrinsic feature of ARPES-spectrum. In term of momentum dispersive curve (MDC) background subtracting, it can simply perform subtracting the spectra by a curve located outside and far away from fermi-momentum (k_F) for all EDCs. In term of energy dispersive curve (EDC) background signal, the energy integrated intensity is small specific momentum (Δk) will be considered as EDC background curve. The analysis details will be provided in the chapter IV.

3.5 DFT calculation

For theoretical investigation, the density functional theory (DFT) calculation was performed to illustrate the electronic structure of NiO. The calculation was calculated by using the Quantum Espresso Package (Giannozzi et al., 2009). The calculation is based on density functional theory in the framework of generalized-gradient approximation with Perdew-Burke-Ernzerhof (PBE) exchange correlation functional (Perdew, Burke and Ernzerhof, 1996). The L(S)DA or spin-polarized calculation is implemented to satisfy the antiferromagnetic nature of NiO. The plan wave cut-off 40 Ry is chosen for the self-consistent calculation. The $4 \times 4 \times 4$ Monkhorst-Pack special k point mesh is included for Brillouin zone sampling. The simplified DFT calculation can be illustrated as presented in Figure 3.5.

More precisely, the LDA+U, an extension of the density functional theory (DFT) approach that addresses the limitations of standard DFT in accurately

describing systems with localized electron-electron interactions is investigated. Specifically, an on-site Coulomb interaction term (U) is added to the DFT Hamiltonian, which allows for a more realistic treatment of localized electron-electron interactions. This term is usually applied to specific orbitals or atomic sites where strong electron correlations are expected, such as transition metal d or f orbitals. LDA+ U calculations require the determination of appropriate values for the Hubbard U parameter. These values are typically obtained from experimental or theoretical studies or through fitting to experimental data. The choice of U values is crucial, as it can significantly impact the calculated electronic structure and properties of the material under investigation. More details on the input file of the planewave self-consistent field (PWscf) are provided in appendix.

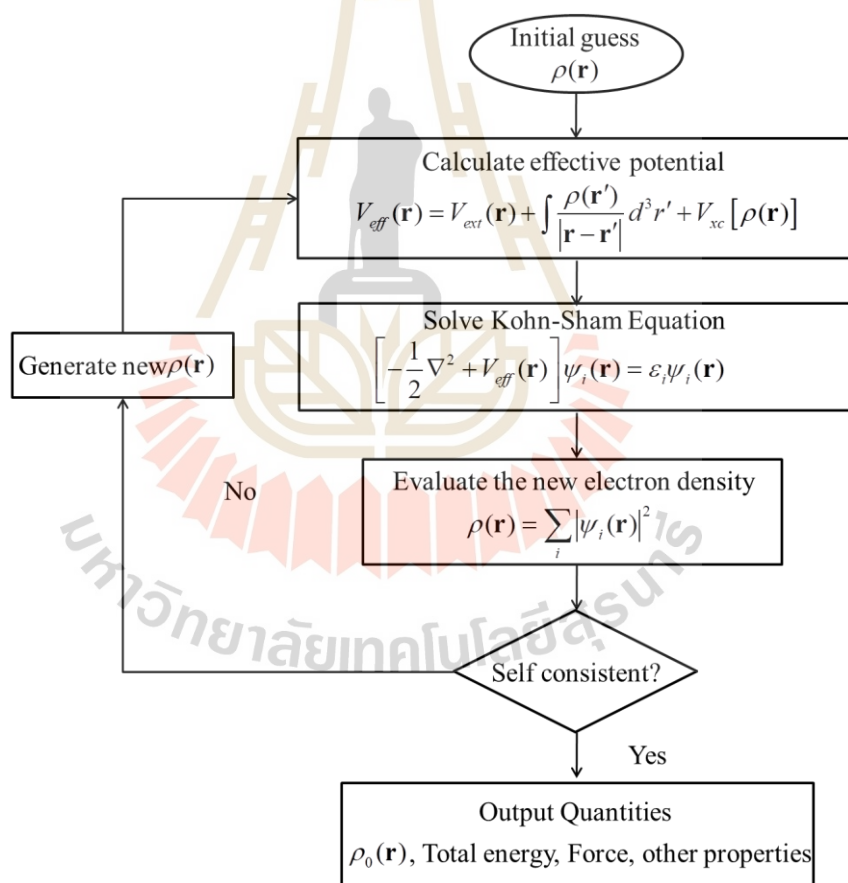
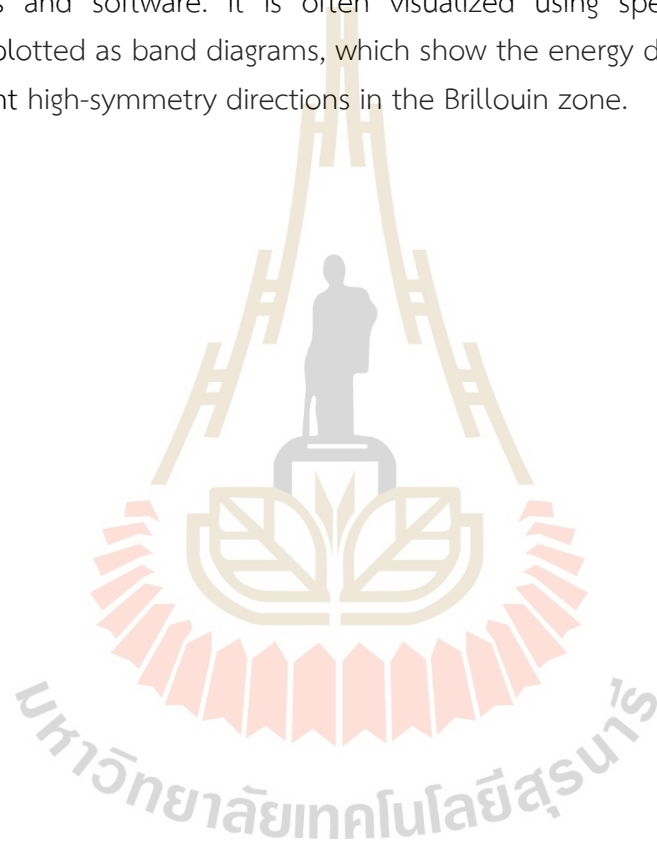


Figure 3.5 Schematic of the self-consistent field scheme for DFT calculation.

To illustrate the electronic band structure, the 'bands' calculation with the set of k points represented the path between the high symmetry point in Brillouin zone is performed. To sum up, the 'scf' is firstly performed to iteratively solves the

Kohn-Sham equations until self-consistency is achieved, and then followed by 'bands' to investigate the band structure in specific k-path direction. These calculations are done by using the PWscf executable (pw.x) which included in the Quantum ESPRESSO software package. In the post-processing stage of electronic structure calculations, the analysis of band structures is typically performed using the bands.x executable. The purpose of bands.x is to read the eigenvalues corresponding to each k-point in the Brillouin zone and format them appropriately for further analysis and visualization. The output of bands.x can be further analyzed using various tools and software. It is often visualized using specialized visualization packages or plotted as band diagrams, which show the energy dispersion of electrons along different high-symmetry directions in the Brillouin zone.



CHAPTER IV

ARPES RESULT

In this chapter, the result from experimental ARPES investigation is presented to illustrate the evolution on electronic structure of NiO upon alkaline metal evaporation. It will be covered with the background subtraction as the data processing procedure. The posted process data are then visualized to identify the relative shifting of the valence band upon the electron surface doing (via alkaline metal evaporation).

4.1 ARPES background subtraction

The ARPES data from the experimental APES study on electronic structure of NiO upon alkaline-metal evaporation are post-processed in term of background subtraction. The aim is to disclose the main feature and make a clear illustration for comparison purpose.

Momentum Distribution Curve (MDC) is a representation of the photoelectron intensity as a function of momentum. It is obtained by integrating the photoelectron intensity over a narrow energy range centered at a particular energy value. By plotting the intensity as a function of momentum, one can visualize the dispersion of the electronic states in the material. The MDC background refers to the background contribution present in the momentum distribution curves. The background can obscure or distort the true electronic structure information contained in the MDCs. To extract reliable information from the MDCs, it is essential to subtract the background contribution. This is typically achieved by fitting a smooth function to the background region in the MDC and subtracting it from the raw data. The choice of the background function depends on the specific experimental setup and the nature of the background sources. Various empirical or theoretical models can be used for background subtraction, such as polynomial functions, Lorentzians, or Gaussian functions. Here, we determine the MDC background by averaging MDC above the Fermi level. This MDC is regarded as the representative of MDC background. Mathematically, we fit the MDC background by polynomial function to achieve the smooth MDC background. The MDC background for the bare NiO single crystal from our experimental measurement can be illustrated as presented in Figure 4.1 and 4.2.

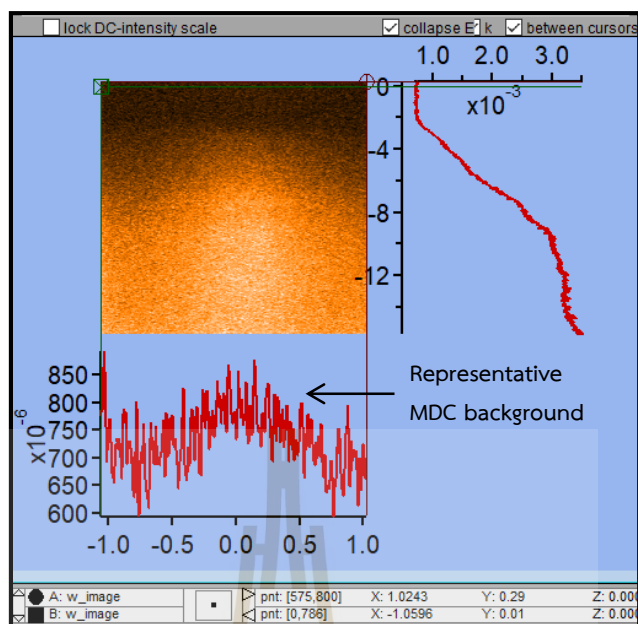


Figure 4.1 User interface panel in iphoto macro present the selected area (above E_F) for MDC averaging.

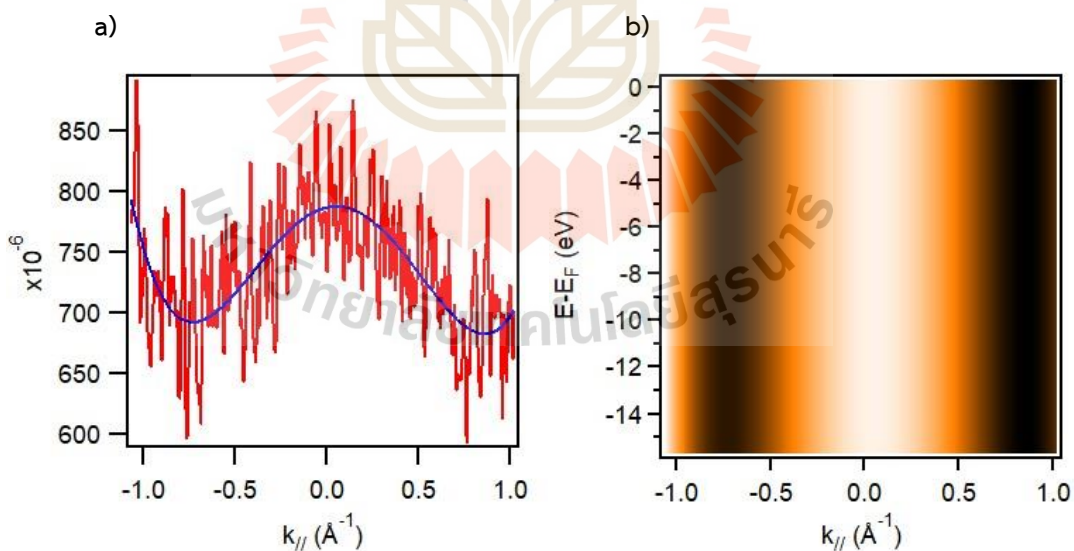


Figure 4.2 The MDC background characterized from the averaged MDC spectrum above the Fermi-level. a) The averaged MDC background (red) is represented by the fitting curve (blue). b) The generated MDC curve for background subtraction from the fitting curve.

The EDC stands for Energy Distribution Curve. It is a representation of the photoelectron intensity as a function of energy. EDCs are obtained by measuring the photoelectron intensity at a specific momentum while scanning the kinetic energy of the emitted electrons. The EDC background refers to the background contribution present in the energy distribution curves. Similar to the MDC background, it arises from various sources and can obscure or distort the true electronic structure information contained in the EDCs. The background in EDCs can stem from instrumental effects, such as detector noise, instrumental resolution, or instrumental broadening due to the finite energy and angular resolution of the experimental setup. To extract meaningful electronic structure information from the EDCs, it is crucial to subtract the background contribution. This is typically done by fitting a smooth function to the background region in the EDC and subtracting it from the raw data. The choice of the background function depends on the specific experimental setup and the nature of the background sources.

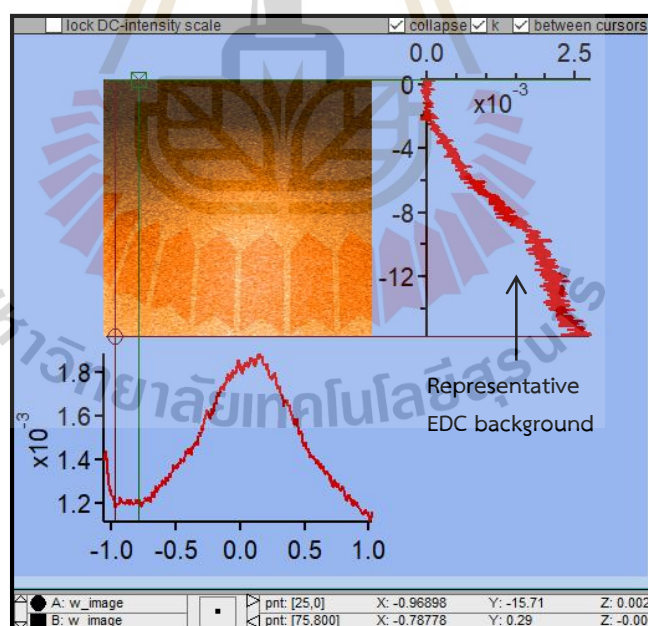


Figure 4.3 User interface panel present the selected area for EDC averaging.

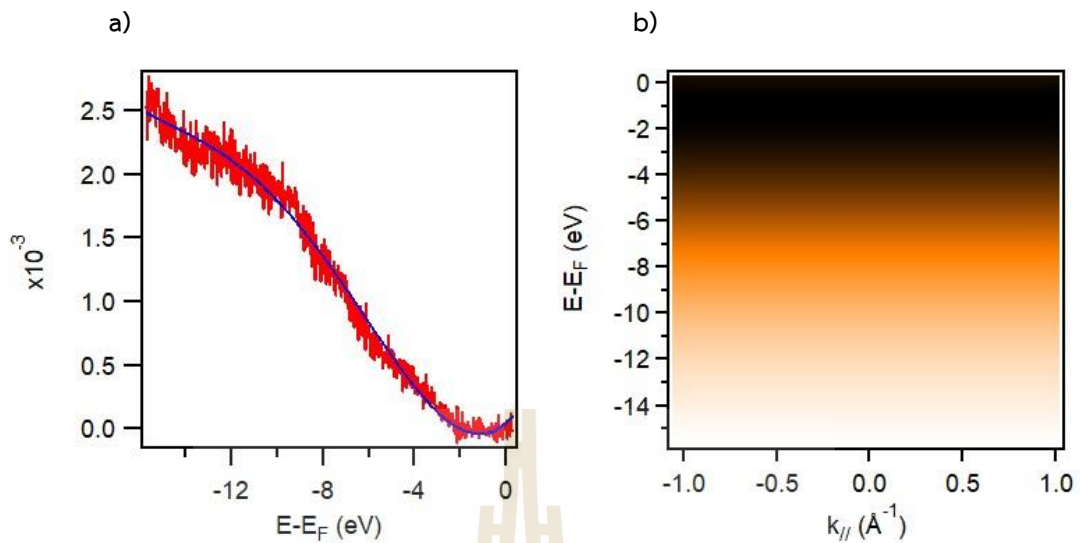


Figure 4.4 The EDC background characterized from the averaged EDC spectrum in a specific momentum range. a) The averaged EDC background (red) is represented by the fitting curve (blue). b) The generated EDC curve for background subtraction from the fitting curve.

4.2 Processed ARPES data

The unprocessed ARPES data for NiO (100) subjected to Potassium Evaporation and UV-shining is illustrated in Figure 4.5 (top panel). It composed of four distinct experimental scenarios: Cleaved NiO, 20-second K-evaporation, 40-second K-evaporation, and 10-minute UV-laser shining. To enhance clarity and facilitate differentiation, the raw data obtained from ARPES undergoes pre-processing steps (involves two main steps: MDC (Momentum Distribution Curve) background subtraction and EDC (Energy Distribution Curve) background subtraction) to enhance the clarity and interpretability of the results as presented in Figure 4.5 (bottom panel). This visualization allows us to further analyze the behavior and characteristics of NiO electronic structure evolution.

To observe the changes in the electronic structure of NiO resulting from potassium evaporation and UV-laser treatment, we extracted Energy Distribution Curve (EDC) spectra for comparison. Figure 4.6 depicts these spectra, revealing an upward shift of the valence band towards the Fermi level (or from higher binding energy to lower binding energy) for both the potassium evaporation and UV-laser

treatment. This particular shift in the band position is analogous to the negative compressibility phenomenon. Based on experimental observations, we speculate that the alteration of correlation effects in NiO due to doping is accountable for the shifting of the chemical potential in this negative compressibility scenario.

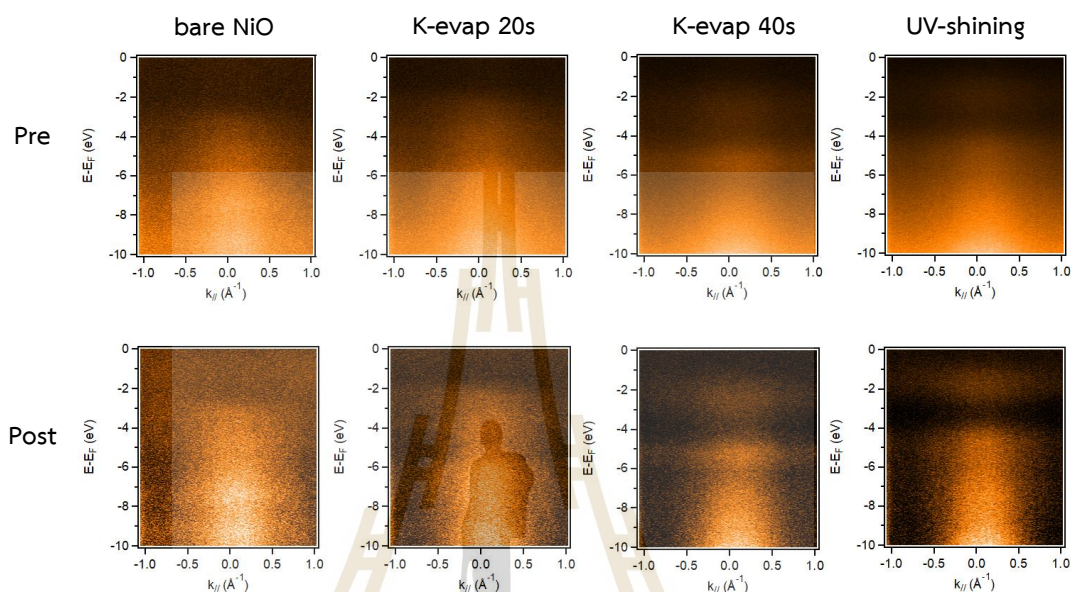


Figure 4.5 Pre-processed (top panel) and Post-processed (bottom panel) ARPES data of the bare NiO, Potassium evaporation (for 20s and 40s), and UV-shining treatment.

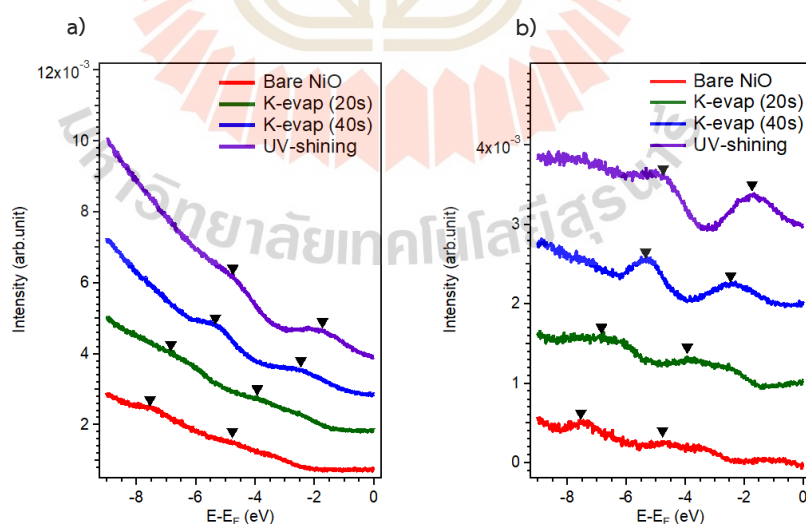


Figure 4.6 The EDC present the relative shifting of the valence band a) the raw data b) the post processed data. Upon the alkaline metal evaporation and UV, the valence band peak shift from the higher binding energy to lower binding energy. This changing in electronic structure is referred as the negative electronic compressibility.

In the theoretical investigation, we perform DFT+U calculation to investigate the electronic structure of NiO. The aim is to visualize the band calculation as the guide line for the experimental ARPES electronic structure observation. The result from band calculation for NiO in the valence band region is plotted as provided in Figure 4.7 (blue line). Besides, the experimental bands are identified, where the lower binding energy band is O2p character and the higher lower binding energy band is the Ni3d character.

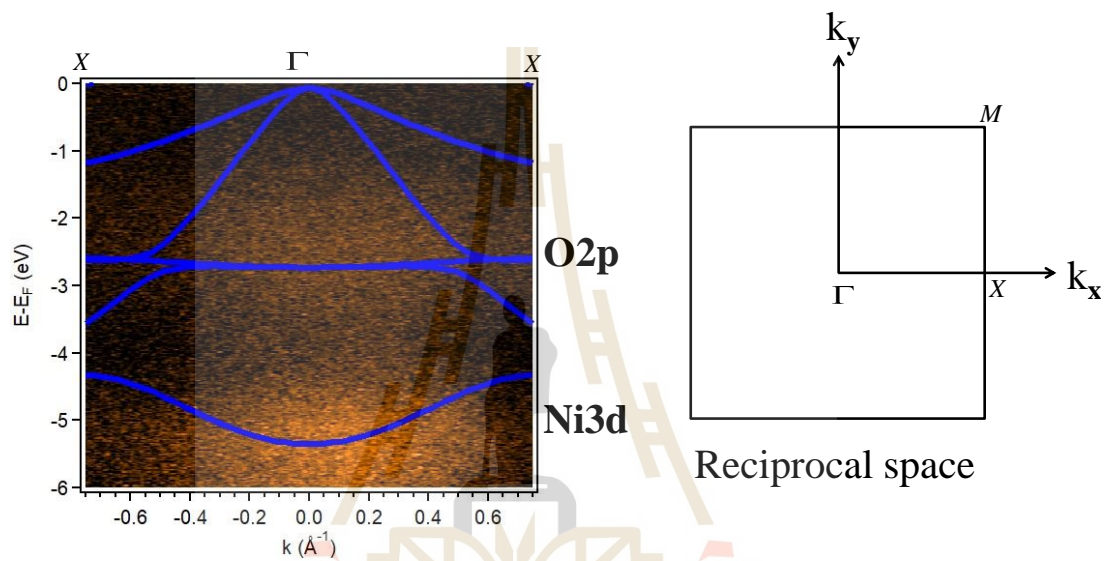


Figure 4.7 The valence band of NiO (100) in the $\bar{x} - \bar{\Gamma} - \bar{x}$, and 2D reciprocal space

To sum up, the comparison across the experimental observation (by the EDC spectrum) gives sufficiently visualization of electronic structure evolution of NiO upon electron doping. The NEC signature are observed in electronic structure evolution of NiO as increasing in electron doing. In other words, this evolution directly results in the negative chemical potential shifting ($\Delta\mu$ is negative, or $d\mu/dn < 0$).

CHAPTER V

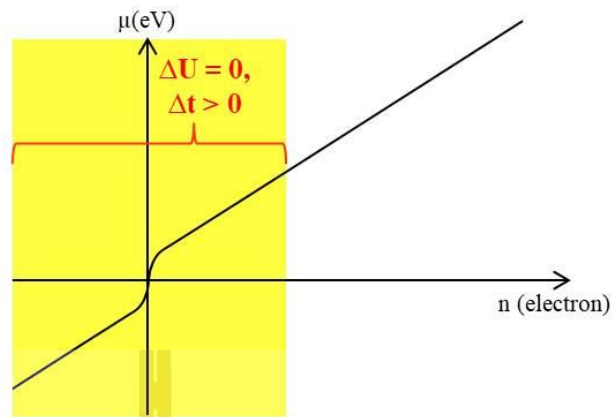
INVESTIGATION OF BATTERY ELECTRODE PERFORMANCE (STRONGLY CORRELATED MATERIALS FRAMEWORK)

This chapter presents our analysis on charge capacity of the battery electrode based on the experimental report data on the galvanostatic charge-discharge measurement. In section 5.1, we start by describes the hypothesis that make a group of Mott-insulator be a good candidate in energy storage application. Then, we will determine the charge storage performance of strongly correlated materials, in particular transition metal oxide (based on literature of the charge/discharge profile) including Cu, Mn, Co, and Fe oxide electrodes. In Section 5.2, the charge storage performance on the copper based electrodes is investigated to distinguish the charge capability of CuO (normal insulator) and Cu₂O (Mott-insulator). In sections 5.3, the manganese based electrodes including MnO₂, Mn₃O₄, and MnO (ranging from insulator to Mott-insulator) are examined to see the variation in charge storage performance. In section 5.4, the cobalt based electrode (CoO, Co₃O₄) and iron based (Fe₂O₃, Fe₃O₄) electrode are described as the complementary cases. Section 5.5 is devoted for the discussion.

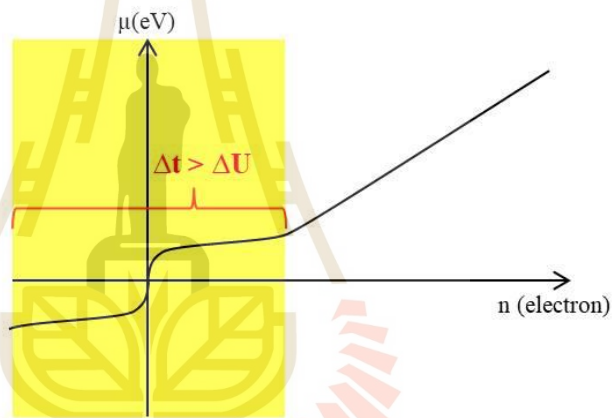
5.1 The Hypothesis

In our model, the chemical potential shifting upon increasing in charge carrier can be simply classified into three categories as illustrated in Figure 5.1. It is composed of increasing in chemical potential (case a), slowly increasing in chemical potential (case b), and decreasing in chemical potential (case c). We propose that slowly increasing and decreasing chemical potential arising from the reduction of Hubbard coulomb interaction (U) upon doping would be the case that can accumulate more charge and yields to the great charge capacity for energy storage application. In order to see the consistency of our hypothesis, we will explore the charge storage of transition metal oxide electrode including Cu, Mn, CO and Fe base electrodes in the section 5.1-5.4.

a) Increasing in μ



b) Slowly increasing in μ



c) Decreasing in μ

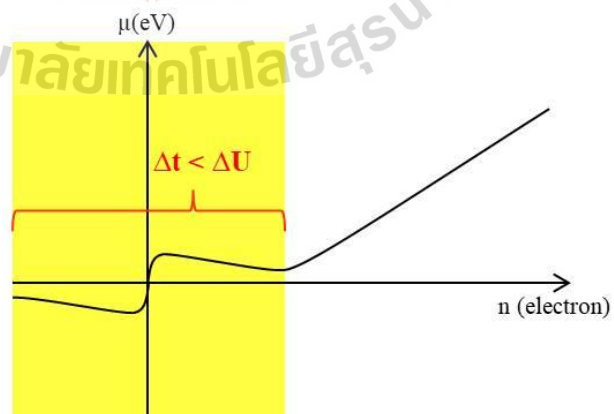


Figure 5.1 The schematic of chemical potential changing.

In Figure 5.1, one can simply assume that the total changing in the chemical potential upon changing in charge carrier is the summation of two terms: intrinsic changing (Δt) and the changing in the decrease in Hubbard coulomb interaction in Mott gap closing scenario (ΔU). The competition between these two terms can be simply interpret into the slowly increasing in chemical potential (Figure 5.1b)) if Δt is greater than ΔU , and decreasing in chemical potential or negative electronic compressibility (NEC) (Figure 5.1c)) if Δt is smaller than ΔU . In term of charge storage capability, the slowly changing in chemical potential (in b)) imply the more ability to accumulate charge as compare to normal increasing in chemical potential (in a)). Moreover, the case of NEC (in c)) would give the ultimate charge storage performance.

5.2 Copper based electrodes (CuO, Cu₂O)

In energy storage, copper-based oxides like Cu₂O and CuO are well-known transition metal oxides used as electrodes. The electronic structure of Cu₂O and CuO can be easily understood by looking at the electron configuration in the d shell of the copper atom. Generally, the copper atom exhibits an electronic configuration of [Ar] 3d¹⁰ 4s¹. For Cu₂O, the formation of chemical bonds results in a d¹⁰ closed shell configuration. Hence, the insulating properties observed in Cu₂O can be explained by the concept of a fully occupied electron or closed shell configuration. Experimental evidence indicates that the band gap of Cu₂O is approximately 2.1 eV. Turn to consider CuO, the electronic configuration of Cu atom exhibits as partial d shell occupation (3d⁹). Turning our attention to CuO, we find that the electronic configuration of the copper atom reveals partial occupation of the d shell, specifically as 3d⁹. Research has shown that the insulating properties of CuO stem from the electron correlation effects within the open-shell d bands (Ghijssen et al., 1988). Studies have determined that the Mott gap of CuO is approximately 1.4 eV. To differentiate the charge capabilities of Cu₂O and CuO, this study compares literature data regarding the capacity of both materials. The discharge characteristics of CuO (Zhang et al., 2015) and Cu₂O (Xiang et al., 2009) have been extracted, as depicted in Figure 5.2. To conduct an analysis, we mathematically determine the capacitance, where the charge capacity is calculated as 70% of the total charge capacity (ΔQ) divided by a specific active potential (ΔV). This ratio is assumed to represent the

effective charge storage capacity and is used to compare the performance of different materials. Typically, the ratio is in the unit of F/g is normalized into F/mol of transition metal atom. The data estimations (ΔQ and ΔV) from the discharge profile and charge storage capacity ($C = \Delta Q / \Delta V$) are summarized and presented in table 5.1.

In comparison, it is found that the charge capacity of CuO (Mott-insulator) is **1.58 times** higher than that of Cu₂O (Band insulator). This relationship is further illustrated and simplified in Figure 5.3. This examination provides valuable insights into the comparative charge capacity of CuO (Mott-insulator) and Cu₂O (Band insulator)

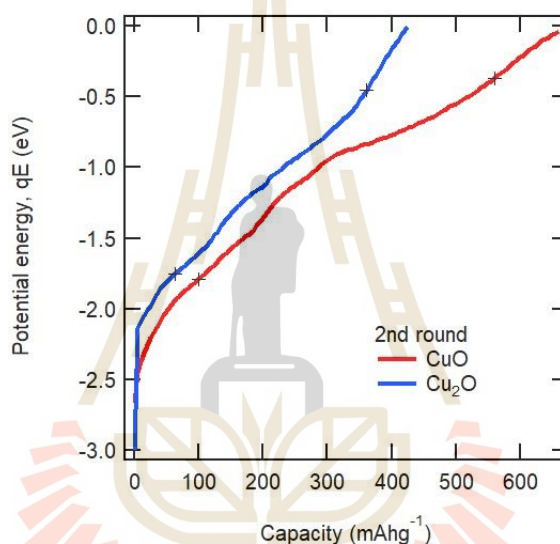


Figure 5.2 The re-reproduced the 2nd round of discharge profile of CuO (red-line) and Cu₂O (blue-line) electrode from experimental researches (Zhang et al., 2015) (Xiang et al., 2009).

Table 5.1 The calculated charge storage capacity of Cu-based electrodes.

Electrode	70% of Max Capacity or ΔQ (mAh/g)	ΔV (Volt)	C (F/g)	C (F/mol of Cu atom)
CuO	462.0	1.42	325	25,880
Cu ₂ O	297.5	1.30	229	16,373

Note: Molecular weight (Mw.) of CuO and Cu₂O are 79.545 and 143.09 g/mol, respectively.

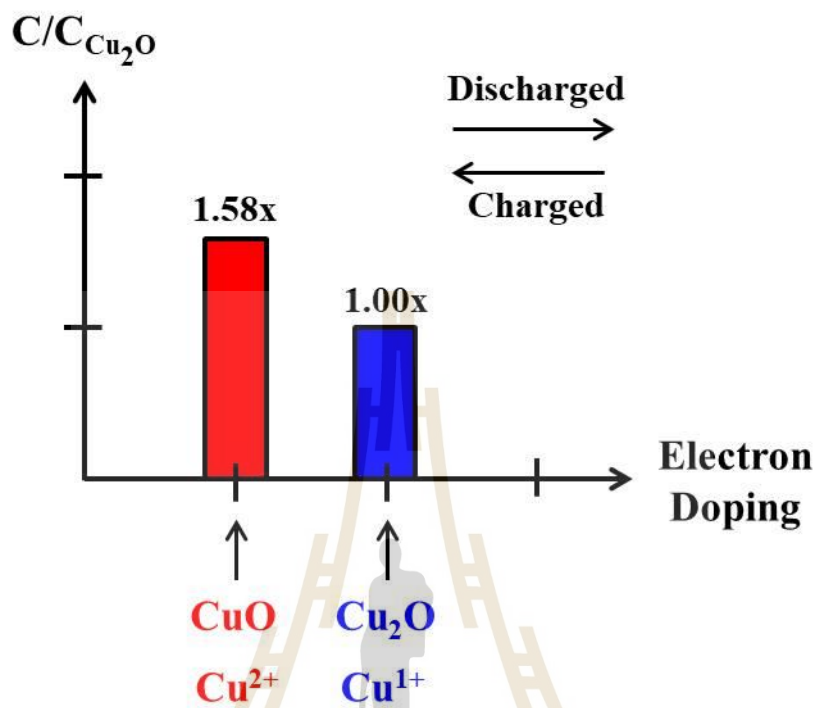


Figure 5.3 The Comparison of the charge storage capacity of CuO (Mott-insulator) and Cu₂O (Band-insulator) electrode (estimated from the reported charge/discharge profile of CuO (Zhang et al., 2015) and of Cu₂O (Xiang et al., 2009)).

5.3 Manganese based electrodes (MnO, Mn₃O₄, and MnO₂)

Manganese oxide electrodes also demonstrate significant potential for application in battery systems. Common forms of manganese oxide include MnO, MnO₂, and Mn₃O₄. The MnO is recognized as a prominent Mott-insulator. It is considered as the archetype of a Mott insulator with perfectly half-filled states, characterized by the Mn (3d⁵) or Mn²⁺ configuration. The MnO₂ is a semiconductor with a partially occupied d shell, specifically with a 3d³ configuration or Mn⁴⁺ state. Likewise, Mn₃O₄ has been identified as a semiconductor. More specifically, MnO₂ and Mn₃O₄ can be considered systems that deviate from the half-filling configuration. In 2014, J. Yue et al., systematically synthesized and investigated the electrochemical performances of various manganese oxides. Based on their experimental discharge profile data, as illustrated in Figure 5.4, the charge storage capacities of MnO, MnO₂, and Mn₃O₄ can be reanalyzed mathematically for comparison purposes. A summary

of the charge storage capacity data for manganese-based electrodes is provided in Table 5.2.

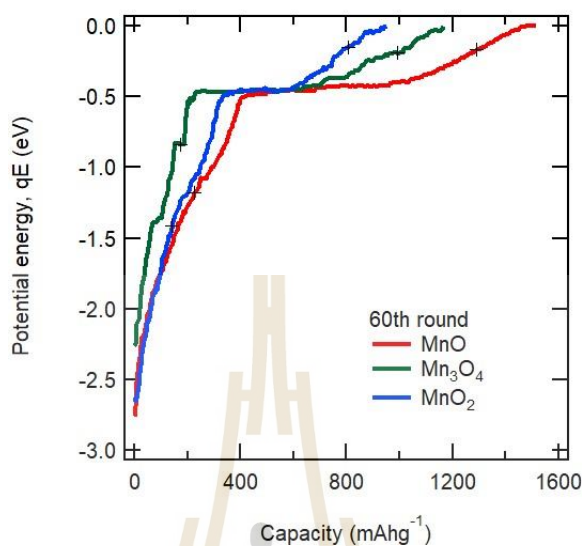


Figure 5.4 The re-reproduced the 60th round of discharge profile of MnO (red-line) and Mn₃O₄ (green-line) and MnO₂ (blue-line) electrode from experimental researches (Yue et al., 2014).

Table 5.2 The calculated charge storage capacity of Mn-based electrodes.

Electrode	70% of Max Capacity or ΔQ (mAh/g)	ΔV (Volt)	C (F/g)	C (F/mol of Mn atom)
MnO	1060.5	1.01	1,054	74,743
Mn ₃ O ₄	815.5	0.65	1,255	95,690
MnO ₂	665.0	1.26	528	45,883

Note: Molecular weight (Mw.) of MnO, Mn₃O₄ and MnO₂ are 70.937, 228.812 and 86.937 g/mol, respectively.

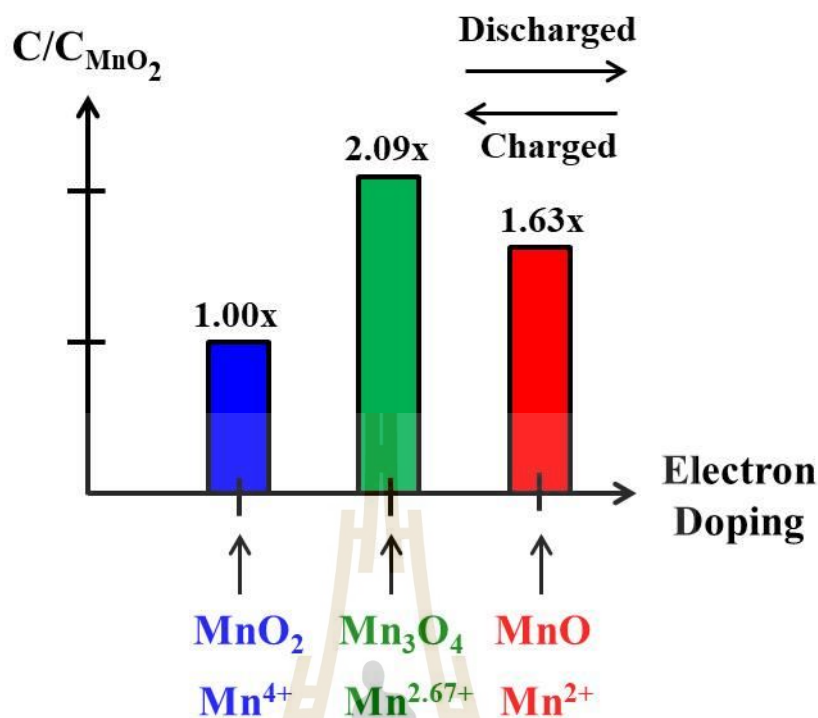


Figure 5.5 The Comparison of the charge storage capacity of MnO₂, Mn₃O₄ and MnO electrode (estimated from the experimental reported charge/discharge profile of Manganese-base electrodes (Yue et al., 2014)).

The investigation revealed that Mn₃O₄ possesses the highest charge storage capacitance among the three manganese oxides. This suggests that Mn₃O₄ has the highest ability to store and release electrical charge compared to MnO₂ and MnO. Interestingly, it has also been noted that the capacitance of MnO (Mott-insulator) is greater than that of MnO₂. The precise reasons behind this phenomenon require further analysis and understanding.

5.4 Cobalt based electrodes (CoO, Co₃O₄) and Iron based electrodes (Fe₂O₃, Fe₃O₄)

We conducted a case study focusing on cobalt (Co) and iron (Fe) based electrodes to further investigate the impact of the relative direction away from the Mott-insulator on the charge storage performance. In our analysis, we referred to the work conducted by Sun et al., 2014 for CoO and Co₃O₄ discharge profiles, and the research by Zhang et al., 2013 for Fe₂O₃ and Y. Pan et al., 2018 for Fe₃O₄ discharge profiles. Analyzing the discharge profiles of different materials, CoO (Mott insulator)

and Co_3O_4 (slight shift to the left of the Mott state) for the cobalt-based electrode, Fe_2O_3 (Mott insulator) and Fe_3O_4 (slight shift to the right of the Mott state) for the iron-based electrode will provide more supporting details. By comparing these profiles, we were able to visualize and evaluate the impact of shifting direction of the Mott-state that gives an opportunity to achieve great charge storage performance.

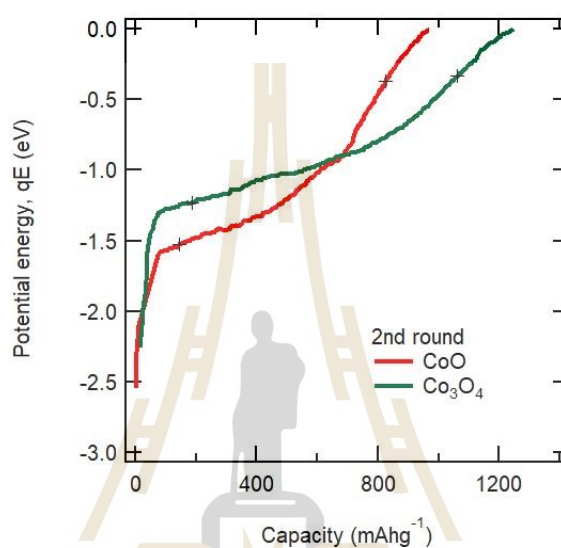


Figure 5.6 The re-reproduced the 2nd round of discharge profile of CoO (red-line) and Co_3O_4 (green-line) electrode from experimental researches (Sun et al., 2017).

Table 5.3 The calculated charge storage capacity of Co-based electrodes.

Electrode	70% of Max Capacity or ΔQ (mAh/g)	ΔV (Volt)	C (F/g)	C (F/mol of Co atom)
CoO	679	1.16	587	44,013
Co_3O_4	875	0.90	978	78,473

Note: Molecular weight (Mw.) of CoO and Co_3O_4 are 74.933 and 240.80 g/mol, respectively.

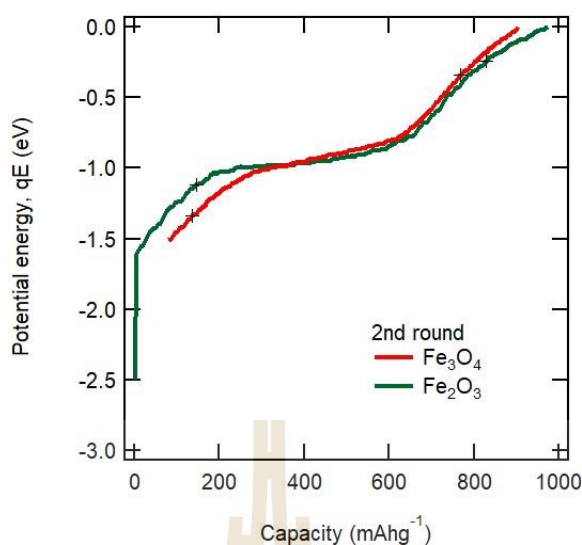


Figure 5.7 The re-reproduced the 2nd round of discharge profile of Fe_2O_3 (green-line) and Fe_3O_4 (red-line) electrode from experimental researches (Zhang et al., 2013)(Pan et al., 2018).

Table 5.4 The calculated charge storage capacity of Fe-based electrodes.

Electrode	70% of Max Capacity or ΔQ (mAh/g)	ΔV (Volt)	C (F/g)	C (F/mol of Fe atom)
Fe_2O_3	682.5	0.88	780	62,279
Fe_3O_4	633.5	1.00	635	49,039

Note: Molecular weight (Mw.) of Fe_2O_3 and Fe_3O_4 are 159.69 and 231.533 g/mol, respectively.

Figure 5.8(a) displays the discharge profiles of CoO and Co_3O_4 , and it can be observed that Co_3O_4 , which is slightly shifted to the left of the Mott-state, exhibits a greater charge storage capacity compared to CoO (Mott-insulator). The estimated capacitance of Co_3O_4 is approximately 1.43 times higher than that of CoO . Figure 5.8(b) illustrates the discharge profiles of Fe_2O_3 and Fe_3O_4 . Notably, Fe_2O_3 , as a Mott-insulator, demonstrates a higher charge capacity, approximately 1.23 times greater than that of Fe_3O_4 (slight shift to the right of the Mott-state).

These findings suggest that the slight shift to the left of the Mott-state has a significant impact on determining the charge storage capacity of electrode materials. This relative shift leads to an enhancement in capacitance, emphasizing the importance of considering the electronic structure and the specific positioning relative to the Mott-state when designing electrode materials for improved energy storage performance.

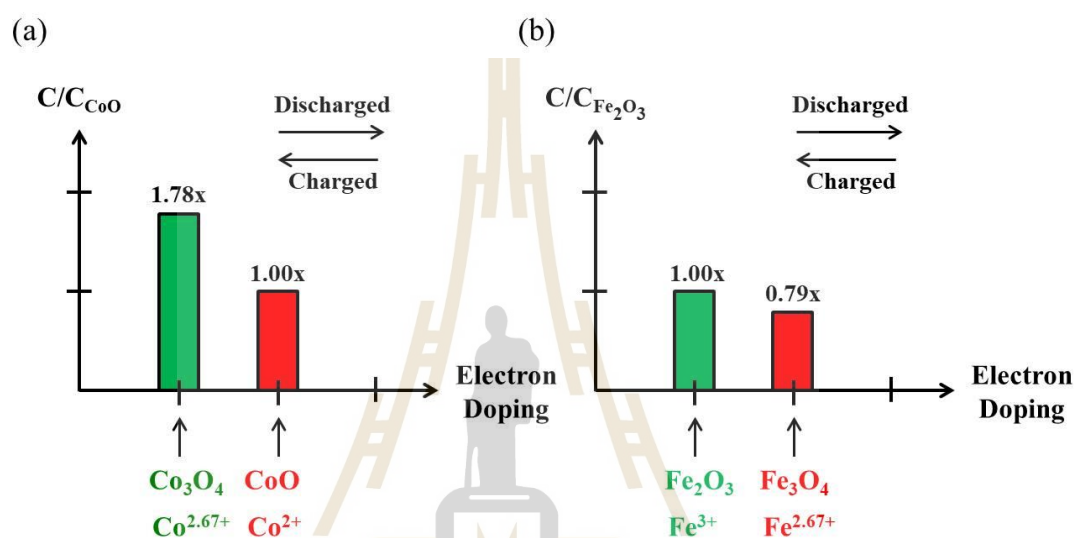


Figure 5.8 The Comparison of the charge storage capacity of (a) Cobalt-based electrode and (b) Iron-based electrode. The red candles (CoO and Fe_3O_4) present the narrow Mott-sweeping, while the green candles (Co_3O_4 and Fe_2O_3) indicate the wide Mott-sweeping. The presented capacitances are normalized by that of the Mott-insulator.

5.5 Discussion on chemical potential shifting

This section aims to provide a generalized overview of the charge storage capacity of strongly correlated materials with a focus on the concept of chemical potential shifting. By discussing this fundamental aspect, we aim to establish a basis for exploring battery electrode materials and understanding their potential for energy storage applications.

It is suitable to focus on the case of manganese base electrode including MnO , Mn_3O_4 and MnO_2 . To gain insights into the charge storage capabilities of manganese-based electrodes, we can begin by analyzing their discharge processes.

By considering a given constant voltage drop (ΔV) as a constraint, we can mathematically evaluate the charge storage capacity of each electrode during discharge, which involves the addition of electrons. The obtained data can then be visualized using a schematic representation of the chemical potential shift, as depicted in Figure 5.9. It is reasonable to expect that the slow variations in the chemical potential of Mn_3O_4 would enable it to store charge more effectively than MnO_2 and MnO .

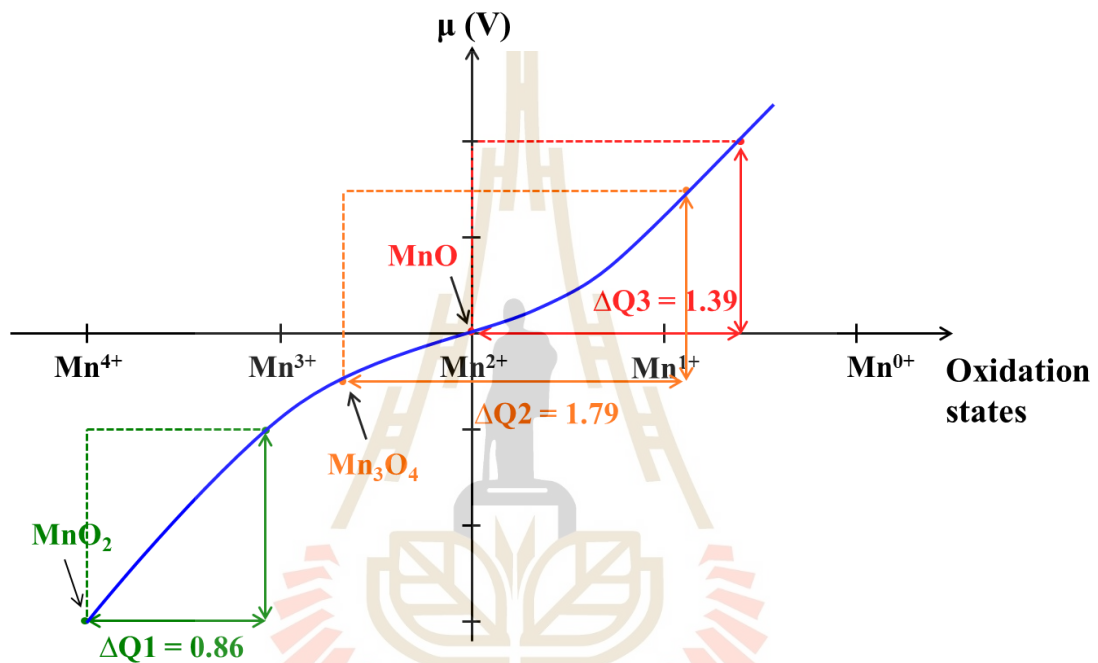


Figure 5.9 The schematic of chemical potential as a function of electron addition in manganese based electrodes.

CHAPTER VI

CONCLUSION AND FUTURE RESEARCH

6.1 Conclusions

The involving in strongly correlated materials and the energy storage application motivate us to investigate and find out the reason to propose the changing scenario in chemical potential shifting that would be good for selected battery electrode. We start by exploring the literature on the experimental observation of the chemical potential shifting in strongly correlated material including LSCO, LSNO, and PCMO (Satake et al., 2000)(Ebata et al., 2008) which provide the chemical potential pinning in some doping range. In addition, Doped correlated materials ($\text{Sr}_{1-x}\text{La}_x$) Ir_2O_7 study by ARPES measurement (Hu et al., 2015) give the illustration of negative chemical potential shifting upon increasing in electron doping. From this literature based data, it inspires us to generalize the chemical potential shift upon carrier doping by the Mott-gap closing assumption. Specifically, doping in the strongly correlated material will decrease the Hubbard coulomb interaction and eventually yield the Mott-gap closing picture.

In term of experimental study, we experimentally investigate the electronic structure of strongly correlated NiO upon increase in electron doping by ARPES. The aim is to distinguish the evolution on electronic structure of strongly correlated material. From the ARPES result, we found the negative shifting in the chemical potential or negative electronic compressibility ($du/dn < 0$). This signature in chemical potential shift would be crucial for battery electrode selection criteria.

In order to give evidence to support the beneficial of strongly correlated material in energy storage application, we introduce the model of chemical potential suppression which occurs in doped Mott-insulator. This suppression in μ raised by the reduction of the Mott-gap upon doping will change the chemical potential to the slowly increasing in chemical potential and make the enhancement in charge storing capability. From data analysis based on the discharge profile of Cu, Mn, Co, and Fe base electrodes, we can conclude that the Mott-state can store more charge than the conventional band insulator. Moreover, the intermediate state (slightly shifted to the left of the Mott-state or in the higher oxidation state of transition metal atom)

gives the highest charge capacity due to the fully utilization of the chemical potential suppression.

6.2 Improvement and future research

To improve the research study, we have to demonstrate more experiment on various samples to cover more range in Hubbard coulomb repulsion (correlation energy). In the further study, we would like to explore the field of material design based on computational material designs. In term of experiment, we are interested in experimental material synthesis by the molecular beam epitaxy (MBE) technique since MBE gives a precise control over the growth of thin films and nanostructures at the atomic level. This enables the deposition of highly uniform and well-defined layers with exceptional accuracy, leading to superior material quality. In order to prove our hypothesis, we would like to synthesis material in the series of doping in Mott-state and experimentally probe the electronic structure evolution directly by ARPES for the entire range across the Mott-state.





REFERENCES

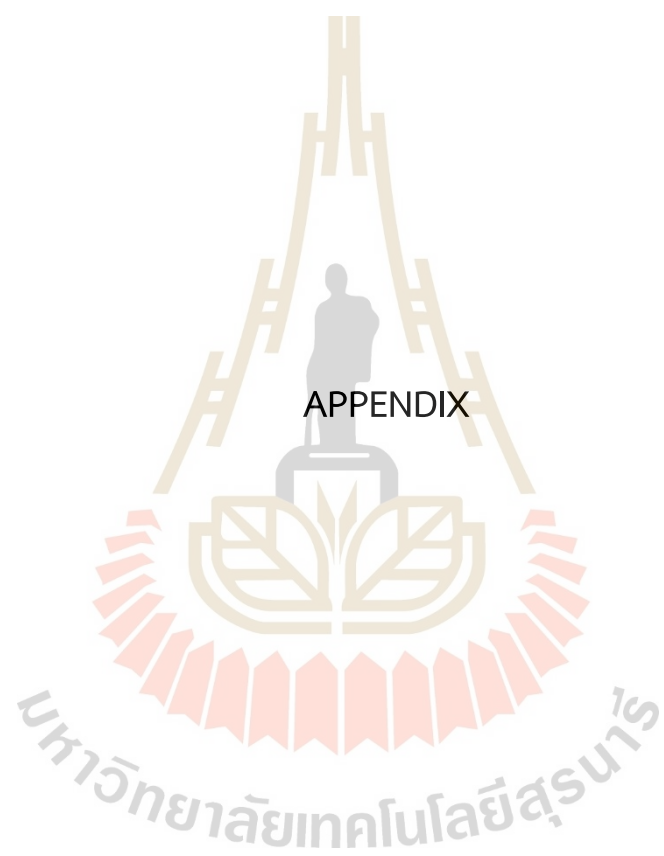
มหาวิทยาลัยเทคโนโลยีสุรนารี

REFERENCES

- De La Torre, A., Walker, S. M., Bruno, F. Y., Riccò, S., Wang, Z., Lezama, I. G., Scheerer, G., Girit, G., Jaccard, D., Berthod, C., Kim, T. K., Hoesch, M., Hunter, E. C., Perry, R. S., Tamai, A., and Baumberger, F. (2015). Collapse of the Mott gap and emergence of a nodal liquid in lightly doped Sr_2IrO_4 . *Physical review letters*. 115(17), 176402.
- Ebata, K., Wadati, H., Takizawa, M., Fujimori, A., Chikamatsu, A., Kumigashira, H., Oshima, M., Tomioka, Y., and Tokura, Y. (2006). Chemical potential shift and spectral-weight transfer in $\text{Pr}_{1-x}\text{Ca}_x\text{MnO}_3$ revealed by photoemission spectroscopy. *Physical Review B*. 74(6), 064419.
- Fujimori, A., Ino, A., Matsuno, J., Yoshida, T., Tanaka, K., and Mizokawa, T. (2002). Core-level photoemission measurements of the chemical potential shift as a probe of correlated electron systems. *Journal of electron spectroscopy and related phenomena*. 124(2-3), 127-138.
- Ghijsen, J., Tjeng, L. H., van Elp, J., Eskes, H., Westerink, J., Sawatzky, G. A., and Czyzyk, M. T. (1988). Electronic structure of Cu_2O and CuO . *Physical Review B*. 38(16), 11322.
- Giannozzi, P., Baroni, S., Bonini, N., Calandra, M., Car, R., Cavazzoni, C., Ceresoli, D., Chiarotti, G. L., Cococcioni, M., Dabo, I., Corso, A. D., Fabris, S., Fratesi, G., Gironcoli, S., Gebauer, R., Gerstmann, U., Gougoussis, C., Kokalj, A., Lazzeri, M., Martin-Samos, L., Marzari, N., Mauri, F., Mazzarello, R., Paolini, S., Pasquarello, A., Paulatto, L., Sbraccia, C., Scandolo, S., Sclauzero, G., Seitsonen, A. P., Smogunov, A., Umari, P., and Wentzcovitch, R. M. (2009). QUANTUM ESPRESSO: a modular and open-source software project for quantum simulations of materials. *Journal of physics: Condensed matter*. 21(39), 395502.
- Hausbrand, R., Cherkashinin, G., Ehrenberg, H., Gröting, M., Albe, K., Hess, C., and Jaegermann, W. (2015). Fundamental degradation mechanisms of layered oxide Li-ion battery cathode materials: Methodology, insights and novel approaches. *Materials Science and Engineering: B*. 192, 3-25.

- He, J., Hogan, T., Mion, T. R., Hafiz, H., He, Y., Denlinger, J. D., Mo, S-K., Dhital, C., Chen, X., Lin, Q., Zhang, Y., Hashimoto, M., Pan, H., Lu, D. H., Arita, M., Shimada, K., Markiewicz, R. S., Wang, Z., Kempa, K., Naughton, M. J., Bansil, A., Wilson, S. D., and He, R. H. (2015). Spectroscopic evidence for negative electronic compressibility in a quasi-three-dimensional spin-orbit correlated metal. *Nature Materials*. 14(6), 577-582.
- Hu, C., Zhao, J., Gao, Q., Yan, H., Rong, H., Huang, J., Liu, J., Cai, Y., Li, C., Chen, H., Zhao, L., Liu, G., Jin, C., Xu, Z., Xiang, T., and Zhou, X. J. (2021). Momentum-resolved visualization of electronic evolution in doping a Mott insulator. *Nature communications*. 12(1), 1356.
- Lee, P. A., Nagaosa, N., and Wen, X. G. (2006). Doping a Mott insulator: Physics of high-temperature superconductivity. *Reviews of modern physics*. 78(1), 17.
- Lv, B., Qian, T., and Ding, H. (2019). Angle-resolved photoemission spectroscopy and its application to topological materials. *Nature Reviews Physics*. 1(10), 609-626.
- Nelson, J. N., Parzyck, C. T., Faeth, B. D., Kawasaki, J. K., Schlom, D. G., and Shen, K. M. (2020). Mott gap collapse in lightly hole-doped $\text{Sr}_{2-x}\text{K}_x\text{IrO}_4$. *Nature Communications*. 11(1), 2597.
- Pan, Y., Zeng, W., Li, L., Zhang, Y., Dong, Y., Ye, K., Cheng, K., Cao, D., Wang, G., and Lucht, B. L. (2018). Surfactant assisted, one-step synthesis of Fe_3O_4 nanospheres and further modified $\text{Fe}_3\text{O}_4/\text{C}$ with excellent lithium storage performance. *Journal of Electroanalytical Chemistry*. 810, 248-254.
- Perdew, J. P., Burke, K., and Ernzerhof, M. (1996). Generalized gradient approximation made simple. *Physical review letters*. 77(18), 3865.
- Satake, M., Kobayashi, K., Mizokawa, T., Fujimori, A., Tanabe, T., Katsufuji, T., and Tokura, Y. (2000). Charge ordering and chemical potential shift in $\text{La}_{2-x}\text{Sr}_x\text{NiO}_4$ studied by photoemission spectroscopy. *Physical Review B*. 61(23), 15515.
- Sawatzky, G. A., and Allen, J. W. (1984). Magnitude and origin of the band gap in NiO. *Physical Review Letters*. 53(24), 2339.

- Sobota, J. A., He, Y., and Shen, Z. X. (2021). Angle-resolved photoemission studies of quantum materials. *Reviews of Modern Physics*. 93(2), 025006.
- Sun, L., Deng, Q., Li, Y., Mi, H., Wang, S., Deng, L., Xiangzhong, R., and Zhang, P. (2017). CoO-Co₃O₄ heterostructure nanoribbon/RGO sandwich-like composites as anode materials for high performance lithium-ion batteries. *Electrochimica Acta*. 241, 252-260.
- Wen, W., Zhao, G., Hong, C., Song, Z., and He, R. H. (2020). 3D negative electronic compressibility as a new emergent phenomenon. *Journal of Superconductivity and Novel Magnetism*. 33, 229-239.
- Xiang, J. Y., Tu, J. P., Yuan, Y. F., Huang, X. H., Zhou, Y., and Zhang, L. (2009). Improved electrochemical performances of core-shell Cu₂O/Cu composite prepared by a simple one-step method. *Electrochemistry Communications*. 11(2), 262-265.
- Yang, X., and Rogach, A. L. (2019). Electrochemical techniques in battery research: a tutorial for nonelectrochemists. *Advanced Energy Materials*. 9(25), 1900747.
- Yue, J., Gu, X., Chen, L., Wang, N., Jiang, X., Xu, H., Yang, J., and Qian, Y. (2014). General synthesis of hollow MnO₂, Mn₃O₄ and MnO nanospheres as superior anode materials for lithium ion batteries. *Journal of Materials Chemistry A*. 2(41), 17421-17426.
- Zhang, J., Sun, Y., Yao, Y., Huang, T., and Yu, A. (2013). Lysine-assisted hydrothermal synthesis of hierarchically porous Fe₂O₃ microspheres as anode materials for lithium-ion batteries. *Journal of Power Sources*. 222, 59-65.
- Zhang, R., Liu, J., Guo, H., and Tong, X. (2015). Synthesis of CuO nanowire arrays as high-performance electrode for lithium ion batteries. *Materials Letters*. 139, 55-58.
- Zhang, S., Zhao, K., Zhu, T., and Li, J. (2017). Electrochemomechanical degradation of high-capacity battery electrode materials. *Progress in Materials Science*. 89, 479-521.



APPENDIX

APPENDIX

INPUT FILE DESCRIPTION OF DFT-CALCULATION

```
&CONTROL
  calculation = 'scf'           ! self-consistence field
  prefix      = 'NiO_af'       ! prepended to input/output filenames
  pseudo_dir  = '/home/chutchawan/qe-7.0/pseudo' ! directory containing pseudopotential files
  outdir      = '/'            ! directory of output files
/
&SYSTEM
 ibrav      = 0                ! bravais-lattice index, 0 = crystal axis defined in CELL_PARAMETERS
  celldm(1) = 7.88             ! lattice parameter (Bohr)
  nat       = 4                ! number of atoms
  ntyp      = 3                ! number of atomic types
  ecutwfc   = 60.0            ! planewave cut-off energy
  nbnd      = 36               ! number of electronic states (bands) to be calculated
  starting_magnetization(1) = 0.0 ! starting spin polarization on atomic type '1', O1
  starting_magnetization(2) = 0.5 ! starting spin polarization on atomic type '2', Ni1
  starting_magnetization(3) = -0.5 ! starting spin polarization on atomic type '3', Ni2
  nspin     = 2                ! spin-polarized calculation
  tot_magnetization = 0.0      ! total majority spin charge - minority spin charge
  lda_plus_u = .true.          ! LDA+U extension
  Hubbard_U(1) = 0.0           ! on-site Hubbard U correction in O1
  Hubbard_U(2) = 4.6           ! on-site Hubbard U correction in Ni1
  Hubbard_U(3) = 4.6           ! on-site Hubbard U correction in Ni2
/
&ELECTRONS
  electron_maxstep = 100       ! maximum number of iterations in a scf step
  conv_thr         = 1.D-6     ! convergence threshold for self-consistency
  mixing_mode      = 'plain'   ! charge density Broyden mixing
  mixing_beta      = 0.7D0     ! mixing factor for self-consistency
  diagonalization  = 'david'   ! davidson iterative diagonalization
```

Figure A Input file for PWscf calculation (Part I).


```

CELL_PARAMETERS alat          ! lattice vectors in units of the lattice parameter or celldm(1)
0.50      0.50      1.00
0.50      1.00      0.50
1.00      0.50      0.50

ATOMIC_SPECIES                ! define atomic species and pseudopotential
O1  15.99 O,pbe-n-rrkjus_psl.1.0.0.UPF
Ni1 58.69 Ni,pbe-spn-rrkjus_psl.1.0.0.UPF
Ni2 58.69 Ni,pbe-spn-rrkjus_psl.1.0.0.UPF

ATOMIC_POSITIONS {crystal}    ! atomic position ( in crystal coordinates)
O1      0.25      0.25      0.25
O1      0.75      0.75      0.75
Ni1     0.0       0.0       0.0
Ni2     0.5       0.5       0.5

K_POINTS {automatic}          ! automatically generated uniform grid of k-points
4 4 4 0 0 0

```

Figure B Input file for PWscf calculation (Part II).

```

&BANDS
prefix      = 'NiO_af'          ! prefix of input file saved by pw.x
outdir      = './'             ! directory of output file
filband     = 'NiO_afbands.dat' ! File contains the bands
/

```

Figure C Input file for band structure analysis.



CURRICULUM VITAE

Name	Mr. Chutchawan Jaisuk
Date of birth	September 5, 1988
Place of birth	Nakhon Phanom, THAILAND
Education	
2016-2023	Doctor of Philosophy (Physics): Ph.D. (Physics) Suranaree University of Technology, Thailand.
2011-2015	Master of Science (Physics): M.Sc. (Physics) Mahidol University, Thailand.
2007-2011	Bachelor of Science (Physics): B.Sc. (Physics) Khonkaen University, Thailand.
Grants and Fellowships	Development and Promotion of Science and Technology Talents Project (DPST)
Academic Experience	
2010	The 7th Siam Photon Science Camp, Synchrotron Light Research Institute, Nakhon Ratchasima, Thailand
2017	Research visit at Advanced Light Source (ALS), Berkeley, CA, USA.
2019	Research visit at Shanghai Synchrotron Radiation Facility (SSRF), Shanghai, CHINA
2019	X-ray Absorption Spectroscopy Workshop, Synchrotron Light Research Institute, Nakhon Ratchasima, Thailand.